Destroying Phantom Jams with Connectivity and Automation:
Nonlinear Dynamics and Control of Mixed Traffic

Tamas G. Molnar
Department of Mechanical Engineering, Wichita State University, Wichita, KS 67260, USA, tamas.molnar@wichita.edu

Gábor Orosz
Department of Mechanical Engineering and Department of Civil and Environmental Engineering, University of Michigan, Ann Arbor, MI 48109, USA, orosz@umich.edu

Abstract. Connected automated vehicles (CAVs) have the potential to improve the efficiency of vehicular traffic. In this paper, we discuss how CAVs can positively impact the dynamic behavior of mixed traffic systems on highways through the lens of nonlinear dynamics theory. First, we show that human-driven traffic exhibits a *bistability* phenomenon, in which the same drivers can both drive smoothly or cause a congestion, depending on perturbations like a braking of an individual driver. As such, bistability can lead to unexpected *phantom traffic jams* which is undesired. By analyzing the corresponding nonlinear dynamical model, we explain the mechanism of bistability and identify which human driver parameters may cause it. Second, we study mixed traffic that includes both human drivers and CAVs, and analyze how CAVs affect the nonlinear dynamic behavior. We show that a large enough penetration of CAVs in the traffic flow can eliminate bistability, and we identify the controller parameters of CAVs that are able to do so. Ultimately, this helps to achieve stable and smooth mobility on highways.

Key words: Connected automated vehicle; mixed traffic; nonlinear dynamics; time delay

1. Introduction

Connected automated vehicles (CAVs) have the promise of revolutionizing transportation, with the ultimate goal of achieving safe, stable and smooth traffic flows. Yet, before the era of fully connected and automated mobility, we can expect at least a few decades of mixed traffic in which CAVs coexist with human-driven vehicles (HVs) on the road. Therefore, it is crucial to prepare CAVs to cooperate with human drivers and to analyze how the behavior of CAVs may impact the dynamics of mixed traffic systems.

There exist several longitudinal control strategies for CAVs that may positively impact the safety and efficiency of mixed traffic. First, *adaptive cruise control (ACC)* systems have been proposed to control auto-
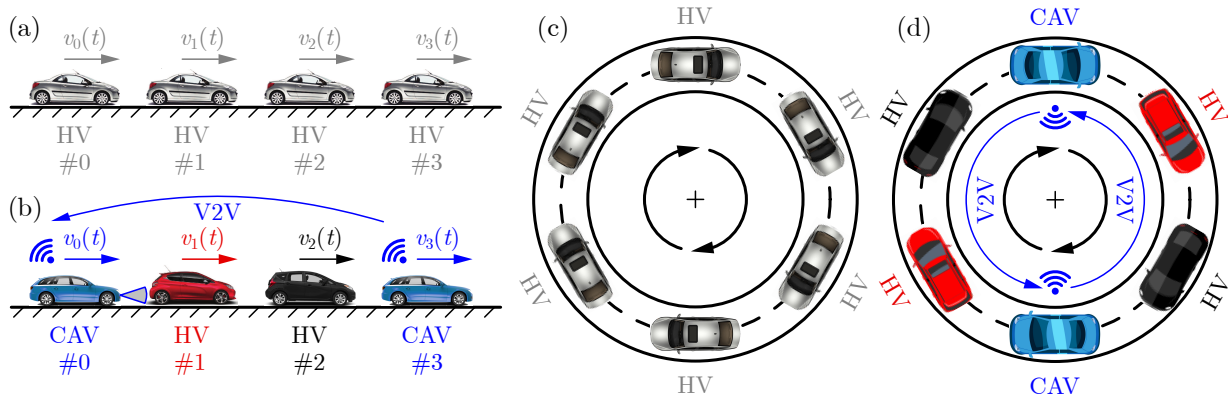
2

Molnar and Orosz: *Destroying Phantom Jams with Connectivity and Automation: Nonlinear Dynamics and Control of Mixed Traffic*
Article submitted to *Transportation Science*

Figure 1 **(a) Illustration of homogeneous traffic consisting of human-driven vehicles (HVs) only. (b) Mixed traffic that includes HVs and connected automated vehicles (CAVs) executing connected cruise control (CCC). (c,d) The corresponding ring configurations that are used for analyzing the nonlinear dynamics of mixed traffic systems.**

mated vehicles by responding to the preceding vehicle in a safe (Nilsson et al. 2016, Ames et al. 2017) and string stable manner (Bekiaris-Liberis et al. 2018, Gunter et al. 2021) with desired driving behavior (Wang et al. 2021, Qin 2022). Later on, ACC systems have been extended to incorporate information from vehicle-to-vehicle (V2V) connectivity that can further improve performance. The approach of *cooperative adaptive cruise control (CACC)* has appeared to regulate platoons of communicating and cooperating CAVs (Turri et al. 2017, Bertoni et al. 2017, McAuliffe et al. 2018, Wang et al. 2018, van Nunen et al. 2019). Although this approach may significantly improve the driving behavior of CAVs, it requires full connectivity and automation within an entire platoon. To control individual CAVs in mixed traffic, the strategy of *connected cruise control (CCC)* (Orosz 2016, Zhang and Orosz 2016) has been proposed, wherein the CAV utilizes information from other connected (but not necessarily automated) vehicles. Importantly, there have been several works that highlighted that the driving behavior of CAVs equipped with the above mentioned controllers can be highly beneficial for the smoothness of mixed traffic (Cui et al. 2017, Čičić and Johansson 2018, Zheng et al. 2020, Giammarino et al. 2021, Hayat et al. 2022, Lichtlé et al. 2022, Wang et al. 2022, Yu and Krstic 2022), which was also demonstrated by experiments (Ge et al. 2018, Stern et al. 2018, Avedisov et al. 2022).

While many of these analyses and control designs have been established by relying on linear dynamical models, traffic systems exhibit several nonlinear dynamics phenomena that can fundamentally shape the overall behavior of vehicles. Some important examples of nonlinearities are: the limited acceleration capabilities of vehicles that imply saturation-type nonlinearities; the relationship between the velocity of vehicles and the distance they intend to keep that is typically nonlinear; and the resistance forces acting on the vehicles (from rolling resistance, road grade and air resistance) that are nonlinear functions of the position and speed. Importantly, such nonlinearities in dynamical systems may cause periodic oscillations

Molnar and Orosz: *Destroying Phantom Jams with Connectivity and Automation: Nonlinear Dynamics and Control of Mixed Traffic*
Article submitted to *Transportation Science*

3

(i.e., so-called limit cycles) that do not exist in linear systems. In the context of vehicular traffic, these periodic motions manifest themselves as repeated, large-amplitude accelerations and decelerations of vehicles, ultimately leading to a traffic congestion also called as *phantom jam*.

Phantom jams have been studied extensively in the literature. The formation of phantom jams in human-driven traffic was explained by Orosz and Stépán (2006) and Orosz et al. (2009, 2010) who used bifurcation analysis tools to study the nonlinear traffic dynamics. It was highlighted that a so-called bistability phenomenon in the underlying dynamics is responsible for the phantom jams, and that the reaction time of human drivers plays a significant role. Kiss et al. (2019) extended these results to analyze the nonlinear dynamic behavior of CAVs executing CCC. The bistability phenomenon was further analyzed, and the effects of connectivity and the limited acceleration capabilities of vehicles were described. These results were established for a three-vehicle scenario: a single CAV and two HVs. Larger-scale mixed traffic scenarios including multiple CAVs have not yet been analyzed from nonlinear dynamics point of view. So far, phantom jams in such scenarios have been studied by simulations: for example, Avedisov et al. (2022) demonstrated the existence of stop-and-go jams in mixed traffic with different penetrations of CAVs.

A comprehensive analysis about the nonlinear dynamics of mixed traffic including multiple CAVs (i.e., different penetrations thereof) is yet to be conducted. Such an analysis is crucial for understanding how CAVs can leverage connectivity and automation to destroy phantom jams. Now we seek to build on the above mentioned previous works to fill this gap. In this paper, we analyze the nonlinear dynamics of mixed traffic with different penetrations of CAVs. This analysis serves to identify controllers for CAVs that provide smooth driving behavior and ultimately mitigate the occurrence of phantom jams. Specifically, we use numerical bifurcation analysis methods to study the nonlinear dynamics of mixed traffic on a ring road setting with multiple HVs and multiple CAVs executing CCC. We study the occurrence of large-amplitude periodic motions corresponding to phantom jams, and we show that CAVs with appropriately designed controllers are able to successfully mitigate and eliminate these unfavorable phenomena.

The paper is organized as follows. In Section 2 we show simulation results to demonstrate the nonlinear behavior of vehicular traffic and motivate the upcoming analysis. In Section 3 we discuss a model of mixed traffic systems, and in Section 4 we describe the underlying linear and nonlinear dynamic behavior. Section 5 closes with conclusions.

2. Motivation

As motivation, we first present numerical simulation results obtained for the homogeneous human-driven traffic shown in Figure 1(a). In particular, the following scenario is simulated. Identical HVs follow each other on a single-lane straight road. Each vehicle is described by the model (1), (5) and (6) discussed later in Section 3, which is simulated via Matlab's built-in delay differential equation solver `dde23`. According to this model, each vehicle accelerates based on human driver commands subject to a response time τ_i

4

Molnar and Orosz: *Destroying Phantom Jams with Connectivity and Automation: Nonlinear Dynamics and Control of Mixed Traffic*
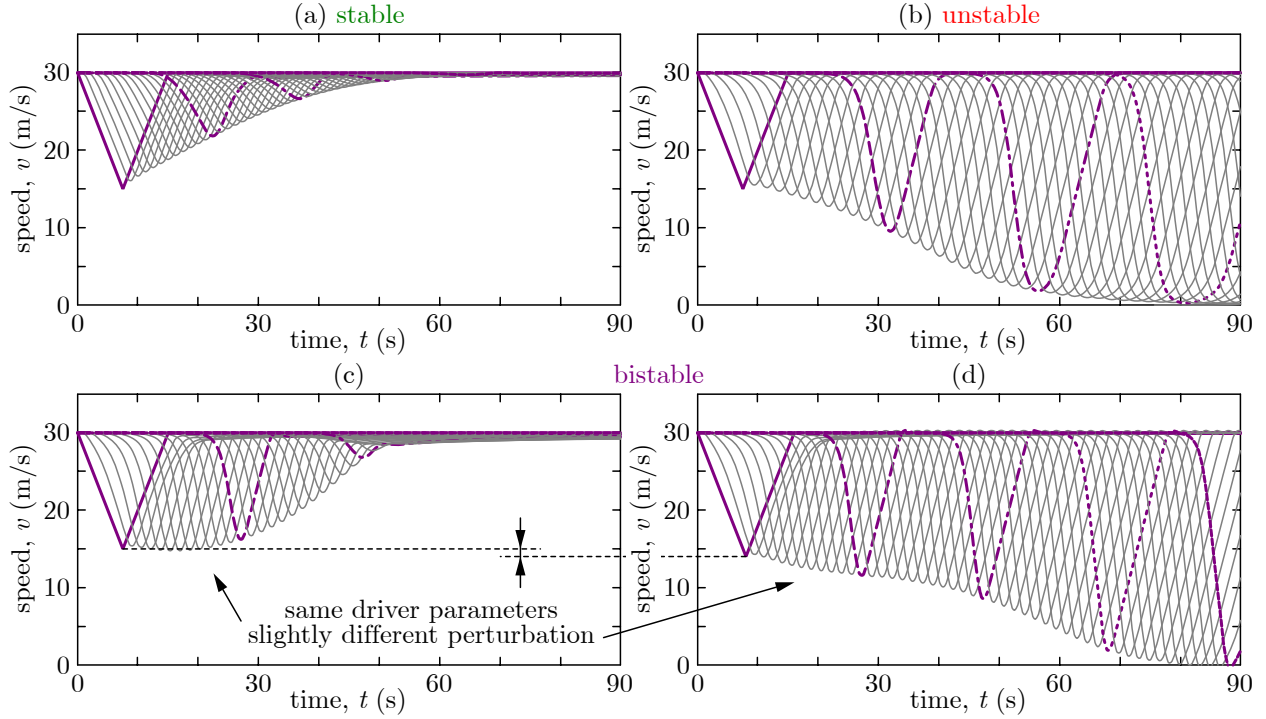Article submitted to *Transportation Science*

Figure 2   Simulation of human-driven traffic. (a) String stable scenario where velocity perturbations decay and smooth traffic is attained. (b) String unstable case where perturbations amplify along the vehicle chain and a stop-and-go traffic jam is formed. (c,d) Bistable scenario where smooth and oscillatory motions both occur, and a phantom jam may be triggered by a large enough perturbation like an excessive braking of an individual vehicle. Importantly, bistability is caused by nonlinearities and cannot be captured by linear models. The model (1), (5) and (6) from Section 3 was simulated with initial conditions $h_i(t) = h_{go}$, $v_i(t) = v_{max}$, $t \in [-\tau_i, 0]$, **for parameters** $\tau_i = 0.6\,\text{s}$ **and (a)** $\alpha_h = 0.1\,\text{s}^{-1}$, $\beta_h = 0.8\,\text{s}^{-1}$, **(b)** $\alpha_h = 0.2\,\text{s}^{-1}$, $\beta_h = 0.4\,\text{s}^{-1}$, **(c,d)** $\alpha_h = 0.4\,\text{s}^{-1}$, $\beta_h = 0.5\,\text{s}^{-1}$ **(related to points S, U and B in Figure 4(a)).**

and acceleration limits a_{min} and a_{max}. The behavior of human drivers is captured by the so-called optimal velocity model (motivated by Bando et al. (1998); see also Kiss et al. (2019), Avedisov et al. (2022)). This model includes the response of drivers to the headway h_i ahead of their vehicle, to their speed v_i, and to the speed difference from the preceding vehicle. The model contains the following human driver parameters: coefficients α_h and β_h that weigh the responses to headway and speed difference, desired standstill headway h_{st}, free flow headway h_{go}, and speed limit v_{max}. The details and parameters of this model will be further explained in Section 3, while notations are summarized in Table 1, and parameter values are listed in Table 2 and at the figures.

Figure 2 shows simulation results for a chain of 49 HVs, where the speed of each vehicle is plotted as a function of time (with every twelfth vehicle highlighted in purple). The simulations imitate a braking event, in which the leading vehicle slows down, then accelerates to recover its original speed and continues to cruise at that speed, while the subsequent vehicles respond to this perturbation. We investigate how such perturbations affect the smoothness of the overall traffic flow.

Figure 2(a) shows a so-called *string stable* scenario, in which each driver reduces its speed less than the vehicle ahead of it, and hence the perturbation ultimately dies out and a smooth traffic flow is recovered over time. While this phenomenon is desired, it depends on the driving behavior of HVs. Other human drivers (e.g. those with larger reaction time) may overreact to the perturbation and reduce their speeds more than the vehicle ahead of them, resulting in the *string unstable* behavior in Figure 2(b). This leads to large-amplitude oscillations in the speeds of vehicles, and eventually, a traffic congestion with stop-and-go motion.

The onset of a traffic congestion, however, may be hard to predict. While the two cases in Figure 2(a,b) – smooth traffic and congestion – correspond to two different sets of human driver parameters, there exist scenarios in which even the *same drivers* can produce these two qualitatively different behaviors. This is illustrated in Figure 2(c,d) where the same human drivers are simulated but the perturbation is different: the lead vehicle reduces its speed by 15 and 16 m/s, respectively. The simulation highlights that a large enough perturbation triggers a traffic congestion, while the traffic flow smoothes out for a small perturbation. This phenomenon is called *bistability*, and the corresponding hard-to-predict congestion is a *phantom jam*.

Clearly, bistability is undesired as it can lead to unexpected phantom jams due to events like a braking of an individual driver. Importantly, bistability phenomena are unique to nonlinear dynamical systems. Thus, nonlinearities – like the saturation of accelerations of vehicles or the nonlinear relationship between the desired speed and distance of HVs – have crucial role in shaping the overall traffic behavior. In what follows, we seek to mitigate unstable and bistable behaviors by injecting CAVs into the traffic flow. We analyze the nonlinear dynamics of mixed traffic and explain the mechanism of bistability, with the end goal of controlling CAVs to achieve globally stable traffic without phantom jams.

3. Modeling of Mixed Traffic

First, we formulate a dynamical model for single-lane mixed traffic systems illustrated in Figure 1. Panel (a) shows the reference case of homogeneous traffic consisting of human-driven vehicles (HVs) only. Panel (b) indicates the case of interest: mixed traffic that includes HVs and connected automated vehicles (CAVs). Such car-following systems are often considered on ring roads for the purpose of analyzing linear and nonlinear dynamics, since the stability properties of large rings can approximate the string stability properties of infinite straight roads (Orosz et al. 2010, Cui et al. 2017, Giammarino et al. 2019, von Allwörden and Gasser 2021, Molnár et al. 2023). The ring configurations corresponding to homogeneous and mixed traffic are shown in panels (c) and (d). Note that the same 3-vehicle group is repeated along the ring in panel (d).

To construct a dynamical model, we use the notations summarized in Table 1. Let us number the vehicles with index i that increases in the direction of motion, and let us denote the set of indices of HVs and CAVs by I_{HV} and I_{CAV}. Furthermore, let v_i denote the velocity of vehicle i and h_i be the headway ahead of vehicle i. We capture the longitudinal motion of these vehicles by delayed double integrator models:

$$\frac{\mathrm{d}h_i}{\mathrm{d}t}(t) = v_{i+1}(t) - v_i(t),$$
$$\frac{\mathrm{d}v_i}{\mathrm{d}t}(t) = \mathrm{sat}(u_i(t - \tau_i)).$$
(1)

Table 1   Notations used throughout the paper.

Variable	Symbol	Variable	Symbol	Variable	Symbol
vehicle index	i	time delay	τ	HV range policy	V_{h}
time	t	saturation function	sat	HV driver parameter	
headway	h	braking limit	$a_{\min}$	(response to headway)	α_{h}
speed	v	acceleration limit	$a_{\max}$	HV driver parameter	
desired acceleration	u	car-following law	f	(response to speed diff.)	β_{h}
number of vehicles	N	speed limit	$v_{\max}$	CAV range policy	V
net ring length	L	standstill headway	h_{st}	CAV control gain	
indices of HVs	I_{HV}	free flow headway	h_{go}	(response to headway)	α
indices of CAVs	I_{CAV}	equilibrium speed	v^*	CAV control gain	
number of vehicles that		HV equil. headway	h_{h}^*	(response to speed diff.)	β_j
CAVs may respond to	m	CAV equil. headway	h^*	CAV speed policy	W

Here u_i is the desired acceleration of each vehicle that is realized by the human drivers or low-level CAV controllers. This acceleration is saturated if it lies outside the acceleration limits $-a_{\min,i}$ and $a_{\max,i}$ of the vehicles, as expressed by:

$$\mathrm{sat}(u_i) = \min\{\max\{-a_{\min,i}, u_i\}, a_{\max,i}\}, \tag{2}$$

that is illustrated in Figure 3(a). Furthermore, the time delay τ_i describes the response time of vehicle i, which consists of the actuation (powertrain) delay of the vehicles and the reaction time of human drivers or the communication and feedback delays of CAVs. Note that, instead of delays, first-order lags are also often used in the literature to capture these response times or to approximate the effects of delays. In practice, typically combinations of lags and delays occur. Meanwhile, time delays are known to give rise to bistability in various nonlinear systems (Dombovari et al. 2008, Saha and Wahi 2011, Molnár et al. 2016, Veraszto and Stepan 2017, Beregi et al. 2019, Vörös et al. 2023). Therefore, here we choose to use a single delay for each vehicle in our model to simplify the analysis while still being able to capture bistability.

In the case of a ring configuration with N vehicles, the dynamics (1) are coupled with the periodic boundary condition:

$$v_0(t) = v_N(t), \tag{3}$$

as well as with a constraint that the headways sum up to the net ring length L:

$$\sum_{i=0}^{N-1} h_i(t) = L. \tag{4}$$

The desired acceleration of human drivers is captured by models of the form:

$$u_i = f_i\Big(h_i, v_i, \frac{\mathrm{d}h_i}{\mathrm{d}t}\Big), \quad i \in I_{\mathrm{HV}}. \tag{5}$$

That is, human drivers tend to respond to the headway h_i, velocity v_i and velocity difference $\mathrm{d}h_i/\mathrm{d}t$, according to a selected human driver model f_i that is often nonlinear. Hence, the saturation function sat and the human driver model f_i give rise to nonlinear dynamics that may showcase bistability.
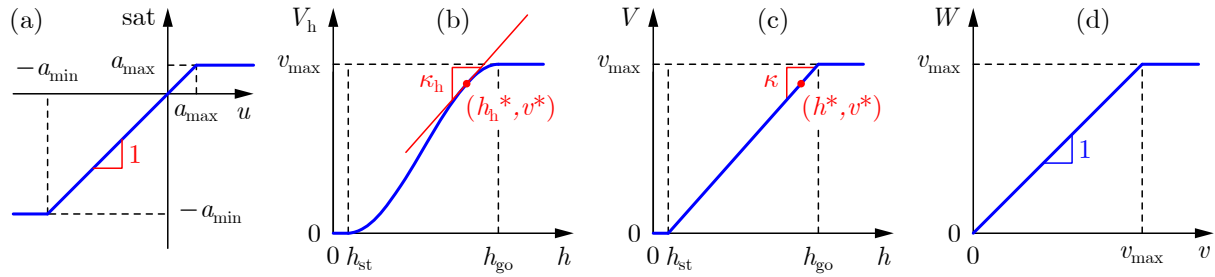
Figure 3 Nonlinearities in the mixed traffic model: (a) saturation of desired acceleration, (b) range policy of human drivers, (c) range policy of CAVs, (d) speed policy of CAVs.

EXAMPLE 1. In the numerical results of this paper (like Figure 2), we use the optimal velocity model (OVM) originated from Bando et al. (1998), which was shown to capture human driver behavior in the experiments of Avedisov et al. (2022). The OVM reads:

$$f_i\Big(h_i, v_i, \frac{\mathrm{d}h_i}{\mathrm{d}t}\Big) = \alpha_{\mathrm{h}}\big(V_{\mathrm{h}}(h_i) - v_i\big) + \beta_{\mathrm{h}}\frac{\mathrm{d}h_i}{\mathrm{d}t}, \tag{6}$$

$\forall i \in I_{\mathrm{HV}}$. This model includes response to the velocity difference $\mathrm{d}h_i/\mathrm{d}t$ with a coefficient β_{h} and response to the headway h_i with a coefficient α_{h}. The latter incorporates the range policy V_{h} that captures the speed that HVs intend to keep as a *nonlinear* function of the headway, such as:

$$V_{\mathrm{h}}(h) = \begin{cases} 0 & \text{if } h \leq h_{\mathrm{st}}, \\ v_{\max}\frac{(3h_{\mathrm{go}} - h_{\mathrm{st}} - 2h)(h - h_{\mathrm{st}})^2}{(h_{\mathrm{go}} - h_{\mathrm{st}})^3} & \text{if } h_{\mathrm{st}} < h < h_{\mathrm{go}}, \\ v_{\max} & \text{if } h_{\mathrm{go}} \leq h, \end{cases} \tag{7}$$

that is plotted in Figure 3(b). This describes that HVs intend to stop if their headway is below the standstill headway h_{st}, while they increase their speed according to a cubic function for larger headways until reaching the speed limit $v_{\max}$ at the free flow headway h_{go}. For simplicity, in numerical examples we consider identical human drivers with the same β_{h}, α_{h} and V_{h} parameters. While the upcoming numerical results are obtained for the OVM and identical HVs, our framework to analyze the occurrence of phantom jams applies to other human driver models and nonidentical driver behaviors as well. Bistability can also be observed for the intelligent driver model and for nonidentical HVs with the OVM, which is demonstrated by simulations in Appendix A.

As opposed to HVs, CAVs are able to respond to multiple vehicles if those vehicles are connected to the CAV. We assume that CAV i is able to detect the preceding vehicle $i + 1$ (by range sensors or V2V connectivity) and that it may connect to up to m vehicles in its communication range. This leads to *connected cruise control* (CCC) laws for CAVs of the form:

$$u_i = f_i(h_i, v_i, v_{i+1}, \ldots, v_{i+m}), \quad i \in I_{\mathrm{CAV}}, \tag{8}$$

8

Molnar and Orosz: *Destroying Phantom Jams with Connectivity and Automation: Nonlinear Dynamics and Control of Mixed Traffic*
Article submitted to *Transportation Science*

Table 2   Parameters used for the numerical results.

Variable	Symbol	Value	Unit
braking limit	$a_{\text{min},i}$	7	m/s^2
acceleration limit	$a_{\text{max},i}$	3	m/s^2
speed limit	v_{max}	30	m/s
standstill headway	h_{st}	5	m
free flow headway	h_{go}	55	m

where, if a distant vehicle $i+j$ (with $1 < j \le m$) is not connected to the CAV, its speed v_{i+j} can be omitted from f_i. The expression of f_i is determined by the CAV's control design. For simplicity, we consider that CAVs respond to the velocities v_{i+j} of distant vehicles, although more general control laws could contain response to positions too.

EXAMPLE 2. In our numerical results, we adopt the CCC strategy from Zhang and Orosz (2016):

$$f_i(h_i, v_i, v_{i+1}, \ldots, v_{i+m}) = \alpha\big(V(h_i) - v_i\big) + \sum_{j=1}^{m} \beta_j\big(W(v_{i+j}) - v_i\big), \tag{9}$$

that is analogous to the OVM (6) with additional response to the velocities of multiple preceding vehicles. This controller was implemented on a passenger vehicle by Ge et al. (2018), Avedisov et al. (2022), Beregi et al. (2023) and on a heavy-duty truck by Alan et al. (2024), with successful hardware experiments on both closed test tracks and public roads. The corresponding control gains α and β_j can be designed, whereas the range policy is chosen to be piecewise linear:

$$V(h) = \begin{cases} 0 & \text{if} \quad h \le h_{\text{st}}, \\ v_{\text{max}} \frac{h - h_{\text{st}}}{h_{\text{go}} - h_{\text{st}}} & \text{if} \quad h_{\text{st}} < h < h_{\text{go}}, \\ v_{\text{max}} & \text{if} \quad h_{\text{go}} \le h, \end{cases} \tag{10}$$

as shown in Figure 3(c). Furthermore, the control law includes the speed policy W that prevents the CAV from speeding if the preceding vehicles exceed the speed limit:

$$W(v) = \min\{v, v_{\text{max}}\}; \tag{11}$$

see Figure 3(d). For simplicity, in numerical examples we choose the controller parameters β, α and V to be the same for all CAVs. Furthermore, we use the same h_{st}, h_{go} and v_{max} values for all HVs and CAVs, listed in Table 2. These parameters, however, could depend on the index i.

4.   Dynamic Behavior of Mixed Traffic

Now we analyze the dynamic behavior of mixed traffic systems by utilizing the model (1)-(11). The analysis is centered around studying the equilibrium and periodic solutions (limit cycles) of this model. For the sake of a simple analysis, we focus on the ring configurations in Figure 1(c,d). However, further below we will demonstrate via numerical simulations that the identified nonlinear phenomena can also be observed for vehicle chains.

Molnar and Orosz: *Destroying Phantom Jams with Connectivity and Automation: Nonlinear Dynamics and Control of Mixed Traffic*
Article submitted to *Transportation Science*

9

The equilibrium of the mixed traffic system describes the scenario where vehicles travel with constant speed, denoted by v^*, while maintaining constant headway, h_{h}^* for HVs and h^* for CAVs. That is, the equilibrium solution is $v_i(t) \equiv v^*$, $h_i(t) \equiv h_i^*$ with $h_i^* = h_{\mathrm{h}}^*$ for $i \in I_{\mathrm{HV}}$ and $h_i^* = h^*$ for $i \in I_{\mathrm{CAV}}$, where $v^* = V_{\mathrm{h}}(h_{\mathrm{h}}^*) = V(h^*)$ holds; cf. Figure 3(b,c). The equilibrium represents the ideal, smooth flow of traffic. The stability of the equilibrium depends on the driving behavior of HVs and CAVs. This is demonstrated by Figure 2(a) and Figure 2(b) that are simulated for different human driver parameters. If the equilibrium is stable, small perturbations like a braking of an individual driver are attenuated as in Figure 2(a), and smooth traffic is attained over time as desired. As opposed, unstable equilibrium results in amplifying perturbations like in Figure 2(b). The stability of the equilibrium is typically studied via linearization, see below.

Periodic solutions, on the other hand, may represent congested traffic. If a traffic congestion forms on the ring configurations of Figure 1(c,d), it typically manifests itself in large-amplitude repeated (periodic) fluctuations in the speeds and headways of vehicles, such as stop-and-go motion. In the nonlinear dynamics literature such periodic motions are called *limit cycles*, which are defined as isolated closed trajectories in the state space. If a limit cycle is stable, then the system tends to this motion over time and large-amplitude velocity fluctuations are showcased in traffic. If the limit cycle is unstable, then the traffic behavior diverges from the corresponding periodic motion (and instead, typically behaviors related to a stable equilibrium or another stable limit cycle are observed over time). The existence and stability of limit cycles are studied through the analysis of the nonlinear dynamics, as discussed below.

Moreover, a stable equilibrium and a stable limit cycle may coexist in certain scenarios (i.e., for certain HV and CAV parameters). This is called *bistability*—defined as the coexistence of two stable solutions in a nonlinear dynamical system with given parameters. The main signature of bistable systems is that they may showcase two qualitatively different behaviors in experiments (related to the two stable solutions) depending on initial conditions and perturbations. In case of bistable traffic, this means that the system converges to the stable equilibrium and showcases smooth traffic flow for small speed perturbations, while it approaches the stable limit cycle and exhibits phantom jam for large perturbations; cf. Figure 2(c,d). That is, both the equilibrium and the limit cycle are locally stable, with a finite domain of attraction determined by the nonlinear dynamics. These properties are quantified for model (1)-(11) below.

4.1. Linear Dynamics

Before addressing nonlinear dynamics, we briefly revisit linear analysis results that neglect nonlinearities. These results were established by linearization of the mixed traffic model (1)-(11) around the equilibrium and by eigenvalue analysis (i.e., studying whether the roots of the corresponding characteristic equation are located in the left half of the complex plane). This linear stability analysis procedure considers small amplitude and arbitrary frequency for the underlying speed perturbations. Through this analysis, Ge and Orosz (2014) established stability conditions at the linear level for the equilibrium of mixed traffic, and expressed these conditions in terms of the parameters of the human drivers and CAV controllers.

10

Molnar and Orosz: *Destroying Phantom Jams with Connectivity and Automation: Nonlinear Dynamics and Control of Mixed Traffic*
Article submitted to *Transportation Science*

Here we briefly outline the steps of analyzing the linearized dynamics, while the remaining details are described in Appendix B. The linearized dynamics are formalized by considering small headway and speed perturbations around the equilibrium, where these perturbations are defined by $\tilde{h}_i(t) = h_i(t) - h_i^*$ and $\tilde{v}_i(t) = v_i(t) - v^*$. Substituting these perturbations into (1) and (5) and linearizing the right-hand side results in the following linear dynamics for HVs ($i \in I_{\text{HV}}$):

$$
\begin{aligned}
\frac{\mathrm{d}\tilde{h}_i}{\mathrm{d}t}(t) &= \tilde{v}_{i+1}(t) - \tilde{v}_i(t), \\
\frac{\mathrm{d}\tilde{v}_i}{\mathrm{d}t}(t) &= A_{i,1}\tilde{h}_i(t - \tau_i) + A_{i,2}\tilde{v}_i(t - \tau_i) + A_{i,3}\frac{\mathrm{d}\tilde{h}_i}{\mathrm{d}t}(t - \tau_i),
\end{aligned}
\tag{12}
$$

where $A_{i,l}$ ($l \in \{1, 2, 3\}$) is the partial derivative of f_i in (5) with respect to its lth argument evaluated at the equilibrium. For the OVM model (6) these coefficients can be expressed using the gains α_{h}, β_{h} and the gradient $\kappa_{\text{h}} = \frac{\mathrm{d}V_{\text{h}}}{\mathrm{d}h}(h_{\text{h}}^*)$ of the range policy; see Appendix B.

Similarly, linearizing (1) and (8) leads to the following dynamics for CAVs ($i \in I_{\text{CAV}}$):

$$
\begin{aligned}
\frac{\mathrm{d}\tilde{h}_i}{\mathrm{d}t}(t) &= \tilde{v}_{i+1}(t) - \tilde{v}_i(t), \\
\frac{\mathrm{d}\tilde{v}_i}{\mathrm{d}t}(t) &= A_{i,1}\tilde{h}_i(t - \tau_i) + A_{i,2}\tilde{v}_i(t - \tau_i) + \sum_{j=1}^{m} A_{i,j+2}\tilde{v}_{i+j}(t - \tau_i),
\end{aligned}
\tag{13}
$$

where $A_{i,l}$ ($l \in \{1, 2, \ldots, m+2\}$) is the partial derivative of f_i in (8) with respect to its lth argument evaluated at the equilibrium. For the controller (9) these coefficients can be expressed using the gains α, β_j, $j \in \{1, \ldots, m\}$ and the gradient $\kappa = \frac{\mathrm{d}V}{\mathrm{d}h}(h^*)$ of the range policy; see Appendix B.

The linearized dynamics can be transformed to Laplace domain. For HVs ($i \in I_{\text{HV}}$), we get:

$$
V_i(s) = T_{i,i+1}(s)V_{i+1}(s),
\tag{14}
$$

whereas for CAVs ($i \in I_{\text{CAV}}$) we obtain:

$$
V_i(s) = \sum_{j=1}^{m} T_{i,i+j}(s)V_{i+j}(s),
\tag{15}
$$

where $V_i(s)$ is the Laplace transform of the velocity perturbation $\tilde{v}_i(t)$. Here $T_{i,i+j}(s)$ are so-called *link transfer functions* (Zhang and Orosz 2016), which characterize the (linearized) response of vehicle i to vehicle $i+j$. The link transfer functions can be expressed using the coefficients $A_{i,l}$; see (20) and (25) in Appendix B.

To describe the overall response of multiple vehicles, the link transfer functions can be combined into a so-called *head-to-tail transfer function* (Zhang and Orosz 2016). For example, for CAVs that respond to m vehicles ahead of them (like in Figure 1(b) where $m = 3$), the head-to-tail transfer function $G_{i,i+m}(s)$ can be used to characterize the overall response of the m vehicles by establishing the relationship between the motions of vehicle i and vehicle $i+m$:
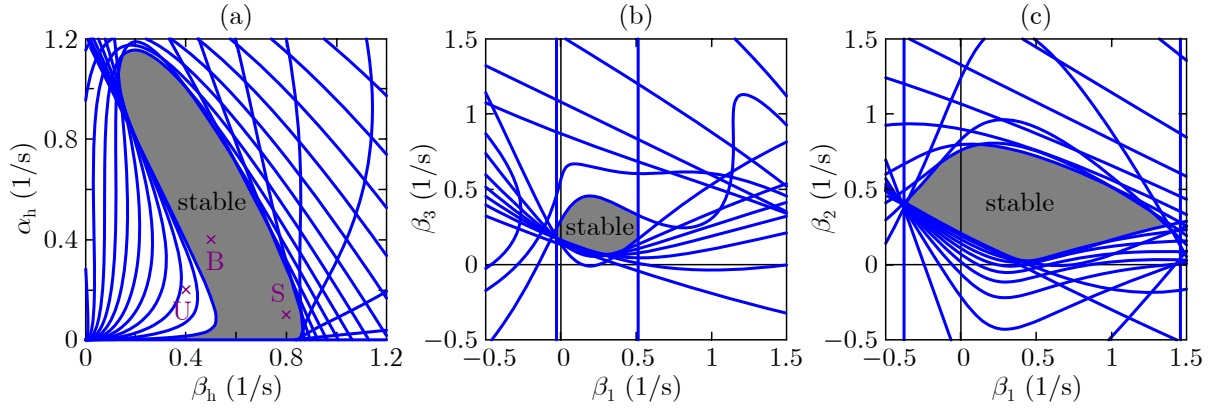
$$
V_i(s) = G_{i,i+m}(s)V_{i+m}(s),
\tag{16}
$$

Figure 4 Linear stability charts of (a) human-driven traffic on a ring, (b) mixed traffic where every third vehicle is CAV, (c) mixed traffic where every second vehicle is CAV. Unfavorable driver behavior may be associated with parameters that yield unstable human-driven traffic. Yet, when a large enough number of CAVs is mixed into the traffic flow, linear stability can still be achieved, provided that the controller parameters of CAVs are chosen from the stable region (grey). The parameters that yield these results are $N = 24$ **and (a)** $\tau_i = 0.6\,\text{s}$**, (b,c)** $\tau_i = 1\,\text{s}$ **(**$i \in I_{\text{HV}}$**),** $\alpha_{\text{h}} = 0.1\,\text{s}^{-1}$**,** $\beta_{\text{h}} = 0.6\,\text{s}^{-1}$**,** $\tau_i = 0.6\,\text{s}$ **(**$i \in I_{\text{CAV}}$**) and** $\alpha = 0.4\,\text{s}^{-1}$**. The net ring length** L **is chosen such that the range policy gradient at the equilibrium headway of HVs is** $\kappa_{\text{h}} = \frac{\mathrm{d}V_{\text{h}}}{\mathrm{d}h}(h_{\text{h}}^*) = 0.6\,s^{-1}$**; cf. Figure 3(b).**

$i \in I_{\text{CAV}}$. The expression of $G_{i,i+m}(s)$ is given in Appendix B. Similarly, the notion of head-to-tail transfer function can also be used to capture the overall response of the N vehicles traveling along the ring configuration:

$$V_0(s) = G_{0,N}(s)V_N(s). \tag{17}$$

Ultimately, the transfer function $G_{0,N}(s)$ can be expressed in terms of the parameters $A_{i,l}$ and the delays τ_i describing the HVs and CAVs, or equivalently, in terms of α_{h}, β_{h}, κ_{h}, α, β_j, κ, and τ_i; see the details in Appendix B.

Using the head-to-tail transfer function that characterizes the linearized response, linear stability analysis can be conducted to determine whether speed perturbations amplify or decay along the ring. The analysis is based on the characteristic equation of the ring configuration:

$$G_{0,N}(s) = 1, \tag{18}$$

which follows from (17) and from $V_0(s) = V_N(s)$ according to the periodic boundary condition (3). The dynamics of the ring configuration are stable and speed perturbations decay if the roots s_ℓ of the characteristic equation (18) are located in the left half of the complex plane, i.e., $\text{Re}(s_\ell) < 0$ holds for all $\ell \in \mathbb{Z}$. Meanwhile, the mixed traffic system is at the boundary of stability when $\text{Re}(s_\ell) = 0$ for some $\ell \in \mathbb{Z}$. This condition is analyzed in Appendix B, and explicit formulas are derived for the stability boundaries in terms of the parameters of HVs and CAVs.

The end result of this analysis is the so-called *stability charts* depicted in Figure 4. These charts distinguish parameters associated with locally stable and unstable equilibrium. Figure 4(a) corresponds to human-driven traffic. If the human driver parameters lie inside the linearly stable region (i.e., the grey shaded domain bounded by the blue curves), the resulting stable behavior qualitatively matches the one observed in Figure 2(a), which was simulated for point S of Figure 4(a). Parameters outside the linearly stable region cause unstable behavior like in Figure 2(b), which was simulated for point U of Figure 4(a). Note, however, that linear stability charts are not able to explain the bistability phenomenon in Figure 2(c,d) associated with point B in Figure 4(a).

Even when human drivers are associated with unstable parameters, linear stability can be achieved if a large enough number of well-designed CAVs is mixed into the traffic flow. Figure 4(b) shows the stability chart of mixed traffic where every third vehicle is CAV (with $m = 3$) while others are HVs associated with unstable parameters, whereas Figure 4(c) represents the case where every second vehicle is CAV (with $m = 2$). Notice that the stable domain grows significantly as the penetration of CAVs increases, which shows the positive impact of CAVs on traffic.

It is important to highlight that the stability charts can be used as a tool for designing the controllers of CAVs in a theoretically justified manner. Since the charts in Figure 4(b,c) showcase linearly stable regions in the space of the CAVs' controller parameters, a stable overall mixed traffic can be achieved by designing controllers such that their parameters lie in the grey shaded stable domain. This method has been successfully implemented and stability charts have been validated by experiments for the case of a single HV-CAV pair by Beregi et al. (2023). In what follows, we seek to derive stability charts for mixed traffic systems by taking into account the phenomenon of bistability. The charts will ultimately allow us to design efficient controllers for CAVs that are able to destroy phantom jams.

4.2. Nonlinear Dynamics

The above described linear stability charts do not contain information about the bistability phenomenon. Now we investigate the nonlinear dynamics and analyze bistability. The analysis is conducted numerically, using a Matlab tool called DDE-BIFTOOL (Engelborghs et al. 2002, Sieber et al. 2014). This tool is able to analyze nonlinear dynamical systems given by delay differential equations, including the calculation of equilibria and their stability, as well as periodic solutions (limit cycles) and their stability. To this end, we implemented the model (1)-(11).

4.2.1. Human-driven Traffic
First we consider the reference case of homogeneous human-driven traffic in Figure 1(c). Figure 5 shows the corresponding results, where the stability chart in panel (a) is repeated from Figure 4(a). In the linearly stable region (union of red and grey domains), the linearized dynamics suggests that the equilibrium traffic flow is stable, hence traffic congestion does not occur. However, analyzing the nonlinear dynamics reveals that large-amplitude oscillatory motions (limit cycles) exist
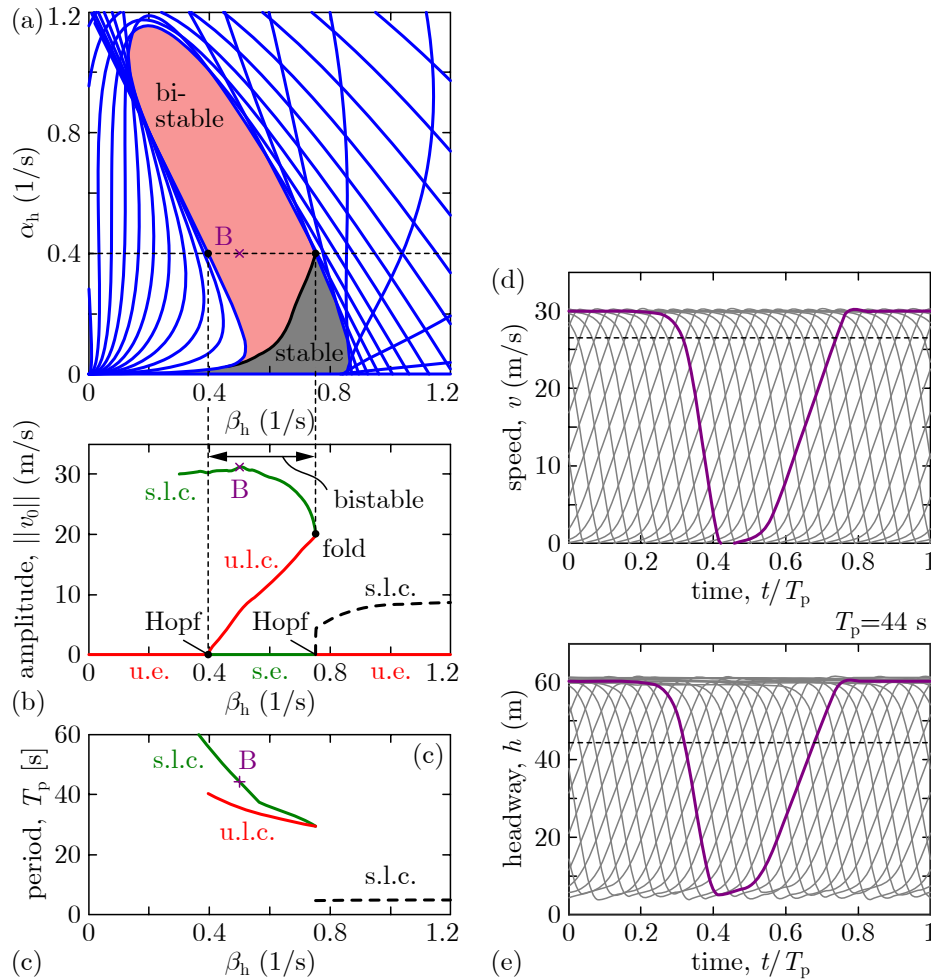
Figure 5   **Nonlinear dynamics of human-driven traffic in ring configuration. (a) Boundaries (blue) of the linearly stable region (shaded red and grey) associated with linearly stable equilibrium traffic, and boundary (black) of the bistable region (shaded red). In the bistable domain, a stable limit cycle coexists with the stable equilibrium, thus perturbations like a braking of an individual driver may trigger oscillatory motions and phantom jams. (b) Amplitude and stability of the arising limit cycles. (c) Time period of limit cycles. (d,e) Large-amplitude oscillatory motion corresponding to the stable limit cycle in point B, which shows the occurrence of a phantom jam. The parameters match those of Figure 4(a).**

for certain parameters. For example, point B(0.5, 0.4) in Figure 5(a) yields such parameters, and Figure 5(d,e) show one period of the corresponding oscillating motion. The motion of one of the HVs is highlighted in purple. Clearly, the velocity and headway undergo large fluctuations that repeat over time as the HV drives around the ring. Remarkably, this stop-and-go phantom jam is revealed through the analysis of the nonlinear dynamics—the linearized dynamics could not predict it.

The above described phantom jam was found systematically through the following analysis. First, we calculated the equilibrium and analyzed its stability numerically for various (β_h, α_h) parameters. This way we reproduced the stability chart in Figure 4(a). We found that along the blue curves in Figure 5(a) the sta-

14

Molnar and Orosz: *Destroying Phantom Jams with Connectivity and Automation: Nonlinear Dynamics and Control of Mixed Traffic*
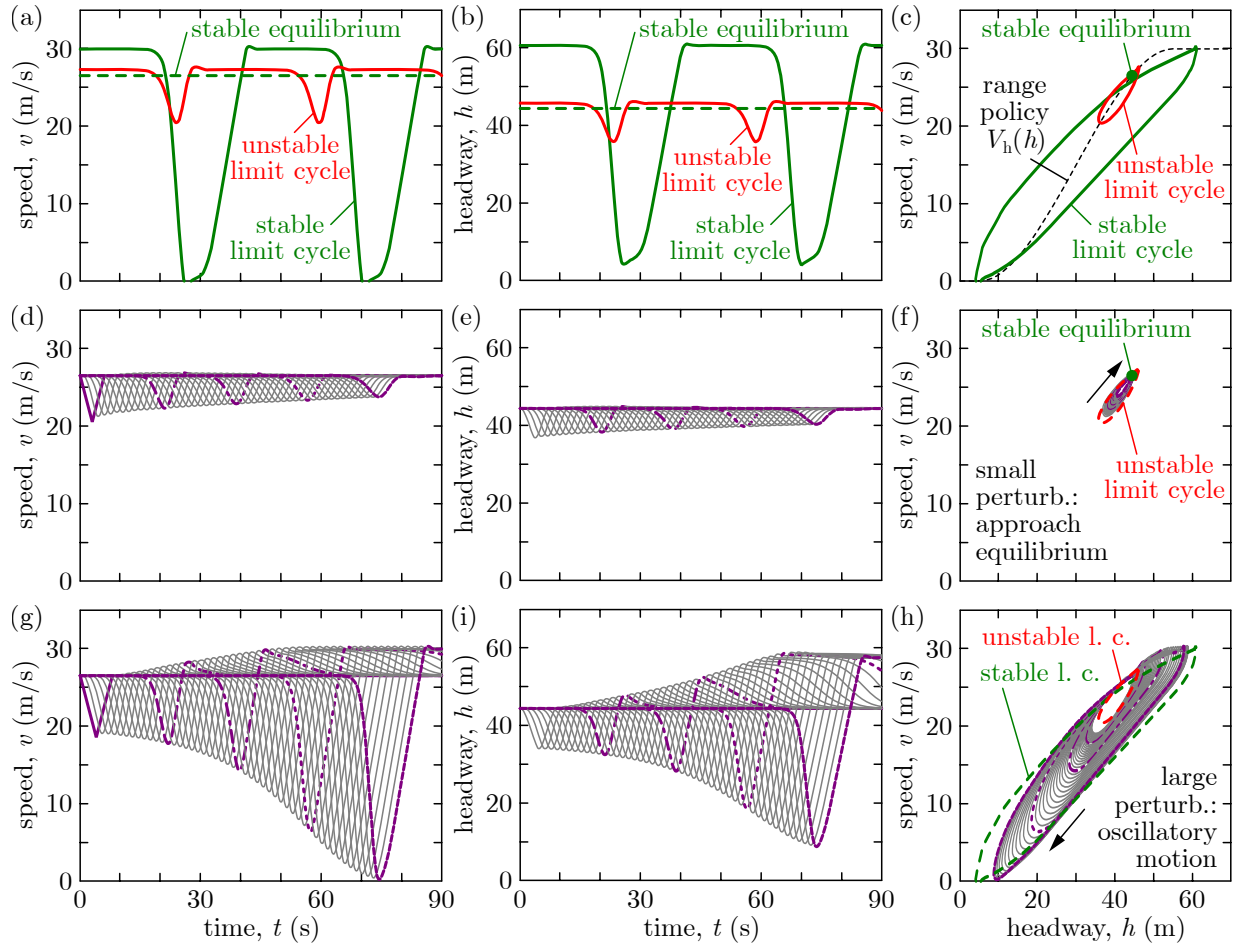Article submitted to *Transportation Science*

Figure 6 **Behavior of bistable human-driven traffic. Equilibrium, unstable limit cycle and stable limit cycle**
coexist for the nonlinear dynamics in ring configuration (top row). Corresponding simulations of an open
vehicle chain show that the traffic flow becomes smooth when responding to a small speed perturbation
(middle row) while it converges to stop-and-go motion for a large perturbation (bottom row). The smooth flow
is associated with the equilibrium, the stop-and-go motion is related to the stable limit cycle, whereas the
corresponding domains of attraction (that determine which one of these two behaviors is observed under
perturbation) are affected by the unstable limit cycle. The parameters are the same as in Figure 2 and point B
of Figure 5(a), while the speed perturbation of the lead vehicle differs from that in Figure 2. The initial
conditions are $h_i(t) = h_{\mathrm{h}}^*$, $v_i(t) = v^*$, $t \in [-\tau_i, 0]$.

bility properties of the equilibrium change as $(\beta_{\mathrm{h}}, \alpha_{\mathrm{h}})$ are varied. Specifically, a so-called Hopf bifurcation happens (that is associated with a complex pair of characteristic roots crossing the imaginary axis and hence a potential change in stability; see Guckenheimer and Holmes (1983)).

Second, limit cycles associated with the Hopf bifurcation were computed. For this calculation, we fixed parameter α_{h} and varied β_{h}; see the horizontal dashed line in Figure 5(a) at $\alpha_{\mathrm{h}} = 0.4\,\mathrm{s}^{-1}$. Limit cycles are born from each Hopf bifurcation point at the intersections of the dashed line and blue curves. We computed these limit cycles for each β_{h} value numerically. This led to branches of limit cycles whose

Molnar and Orosz: *Destroying Phantom Jams with Connectivity and Automation: Nonlinear Dynamics and Control of Mixed Traffic*
Article submitted to *Transportation Science*

15

stability and amplitude (i.e., the peak-to-peak amplitude of the corresponding velocity fluctuations) are indicated in Figure 5(b) as a function of β_{h}. In Figure 5(b), we can observe the occurrence of linearly unstable equilibria (u.e.), linearly stable equilibria (s.e.), unstable limit cycles (u.l.c.) and stable limit cycles (s.l.c.). The branch of limit cycles responsible for the phantom jam is highlighted by colored thick line, while other branches are plotted by dashed black lines. Along the colored branch, first the limit cycles are unstable and their amplitude increases as β_{h} is increased. Then, the branch folds, the limit cycles become stable, and the amplitude saturates around v_{max} as β_{h} is decreased. These large-amplitude stable limit cycles are associated with oscillatory, stop-and-go motion – a phantom jam – where the speed repeatedly changes between 0 and the speed limit v_{max}. The time period of the limit cycles is plotted in Figure 5(c), whereas one period of the stop-and-go motion is illustrated in Figure 5(d,e) for point B of Figure 5(b).

Figure 5(b) reveals that for certain β_{h} parameters—between the Hopf bifurcation point and the point where the branch of limit cycles folds—a large-amplitude stable limit cycle coexists with the stable equilibrium (and also with an unstable limit cycle). The coexistence of the stable equilibrium and the stable limit cycle is called bistability—a phenomenon appearing in nonlinear systems only. It means that in practice two qualitatively different behaviors can be observed for the same human drivers: the traffic flow can either be stable and smooth (associated with convergence to the equilibrium) or a phantom jam can appear (associated with convergence to the large-amplitude stable limit cycle); as illustrated by Figure 2(c,d).

Whether smooth flow or congestion is observed for a bistable traffic system depends on whether perturbations push the system to the domain of attraction (DoA) of the equilibrium or to that of the stable limit cycle. These DoAs are determined by the unstable limit cycle, as highlighted in Figure 6. The top row shows the stable equilibrium, unstable limit cycle and stable limit cycle of the human-driven traffic for point B of Figure 5(a). Note that the stable limit cycle matches the purple curves in Figure 5(d,e). The other panels of Figure 6 show simulations of the corresponding open chain of vehicles with the same parameters; cf. Figure 2(c,d). The middle row shows a below-threshold (6 m/s) speed perturbation for the lead vehicle. As this perturbation is "inside" the unstable limit cycle in the phase portrait of panel (f), convergence to the equilibrium is observed and the traffic flow becomes smooth. Meanwhile, an above-threshold (8 m/s) perturbation in the bottom row goes "outside" the unstable limit cycle in panel (h), and results in convergence to the large-amplitude stable limit cycle associated with a stop-and-go traffic jam. Note that limit cycles were calculated for the ring configuration with $N = 24$ vehicles, whereas simulations were conducted for an open chain of vehicles, hence the agreement between these results is approximate. Furthermore, technically the state space of system (1)-(11) is infinite-dimensional due to the time delay, and the phase portraits in the right panels of Figure 6 are low-dimensional representations only. In fact, the DoAs exist in the infinite-dimensional state space, where it is nontrivial to interpret "inside" and "outside" the unstable limit cycle. Thus, the amplitude, frequency and shape of perturbation signals all play a role in whether a phantom jam

is observed. Nevertheless, the existence of the unstable limit cycle determines the topology of the system and the two DoAs, and ultimately leads to the existence of phantom jams.

Importantly, we found that bistability occurs in human-driven traffic for a relatively wide range of driver behaviors. Specifically, by repeating the limit cycle computation of Figure 5(b) for various values of α_{h}, we identified a large bistable region in the $(\beta_{\mathrm{h}}, \alpha_{\mathrm{h}})$ parameter space, as indicated by red shading in Figure 5(a). Meanwhile, the occurrence of the bistability phenomenon is undesired in traffic systems, as it can lead to unexpected phantom jams. Therefore, next we investigate the occurrence of bistability in mixed traffic, and we seek to mitigate it by CAVs.

4.2.2. Mixed Traffic We repeated the numerical analysis of equilibria and limit cycles for the case of mixed traffic. Figure 7 shows the corresponding results where every third vehicle is CAV (each responding to the CAV $m = 3$ vehicles ahead) while the others are HVs. The dynamic behavior is analyzed as a function of the CAVs' controller parameters. The figure shows that while a bistable region still exists (see panel (a)) where traffic congestion could happen (see panels (d,e) associated with point B(0.25,0.1)), a significant part of the linearly stable region is *not* bistable. Thus, by using this chart, one can easily find controller parameters for CAVs that avoid bistability and ultimately lead to smooth traffic flow—even under nonlinear behavior.

Figure 8 shows the effect of increasing the penetration of CAVs in the traffic flow. As opposed to Figure 7 where every third vehicle was CAV (corresponding to 33% penetration with $m = 3$), Figure 8 shows the scenario in which every second vehicle is CAV (i.e., 50% penetration with $m = 2$). Clearly, more CAVs increase the size of the linearly stable region and reduce the relative size of the bistable region, which both facilitate smooth, congestion-free traffic. Note that Figure 8 reveals an additional phenomenon that is common for larger numbers of vehicles: the occurrence of period doubling (PD) bifurcation that gives rise to a limit cycle with doubled time period; see panel (b) that is plotted for $\beta_2 = 0.1\,\mathrm{s}^{-1}$. These additional period-two limit cycles were also considered when analyzing bistability.

Importantly, Figure 7 and Figure 8 provide a theoretically justified way to select the parameters of the CAVs' controllers. In particular, the control gains associated with globally stable traffic are located inside the grey region of Figure 7(a) and Figure 8(a). Thus, these stability charts offer stable gains for implementation, like the gains in point S. To demonstrate this, we chose the stable point S(0.3,0.3), and we conducted numerical simulations. The simulations are shown in Figure 9 for 17%, 25%, 33% and 50% penetration of CAVs (with $m = 6$, $m = 4$, $m = 3$ and $m = 2$, respectively). While the human drivers behave string unstable (see the growing perturbations for the grey curves), the CAVs (blue) are able to overcome this and smooth out the traffic as desired.

The ability of CAVs to smooth out mixed traffic flows, however, is limited by their penetration. Stable traffic may no longer be achievable if the CAV penetration is too low. The minimum penetration required
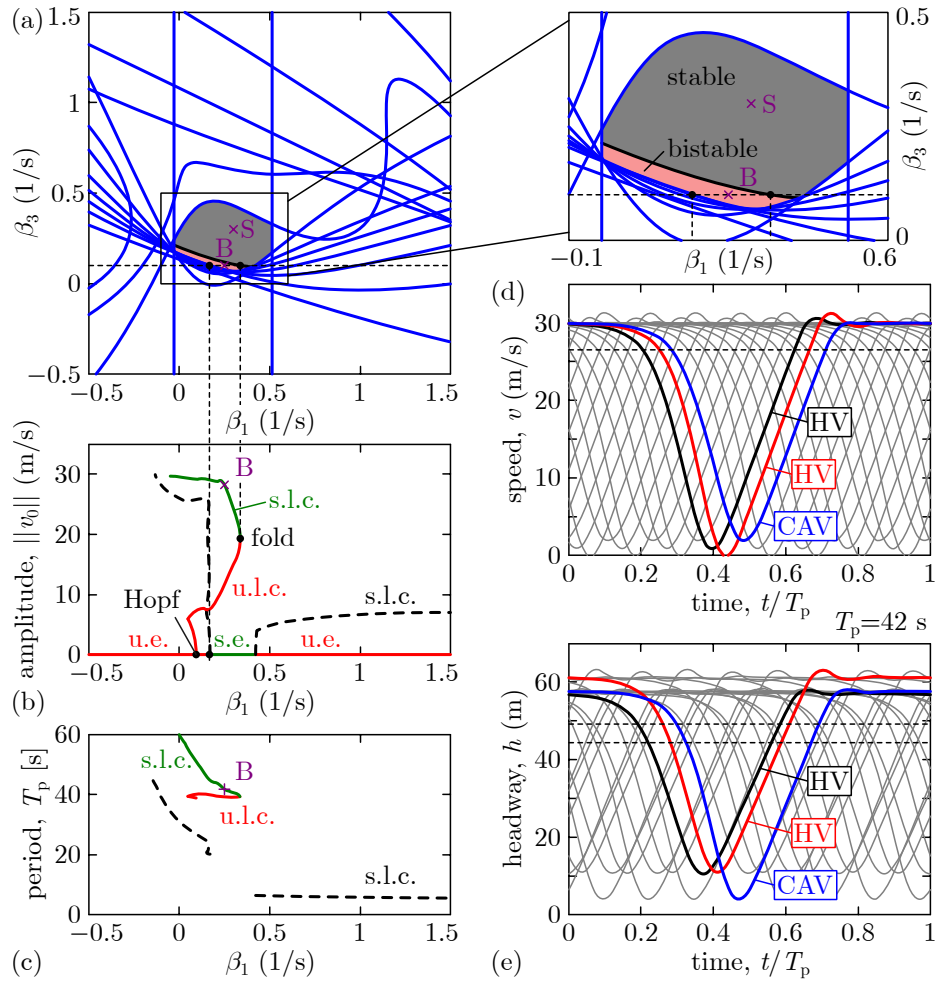
Molnar and Orosz: *Destroying Phantom Jams with Connectivity and Automation: Nonlinear Dynamics and Control of Mixed Traffic*
Article submitted to *Transportation Science*

17

Figure 7 Nonlinear dynamics of mixed traffic in ring configuration where every third vehicle is CAV (with $m = 3$). The same properties are shown with the same notations as in Figure 5. Observe that the bistable region is small, thanks to the CAVs. While a phantom jam with large-amplitude oscillatory motion could still occur, the controller parameters of CAVs can be tuned using this chart to avoid it. The rest of the parameters match those of Figure 4(b).

for stable traffic depends on the human driver behavior. In Figure 9 every human driver has a large reaction time ($\tau_i = 1\,\mathrm{s}$) and hence behaves in a highly string unstable manner, making this a "worst-case scenario". For this particular example, instability is observed below 15% penetration (i.e., for $m \geq 7$).

It important to remark that the connectivity between the CAVs plays crucial role in achieving globally stable mixed traffic. Specifically, connectivity allows CAVs to obtain information from connected vehicles farther ahead, beyond the line of sight. This information provides a look-ahead of the upcoming velocity perturbations, which enables CAVs to respond to perturbations early, and thereby compensate for the time delays involved in their dynamics that would otherwise give rise to the linear instability and nonlinear bistability phenomena.
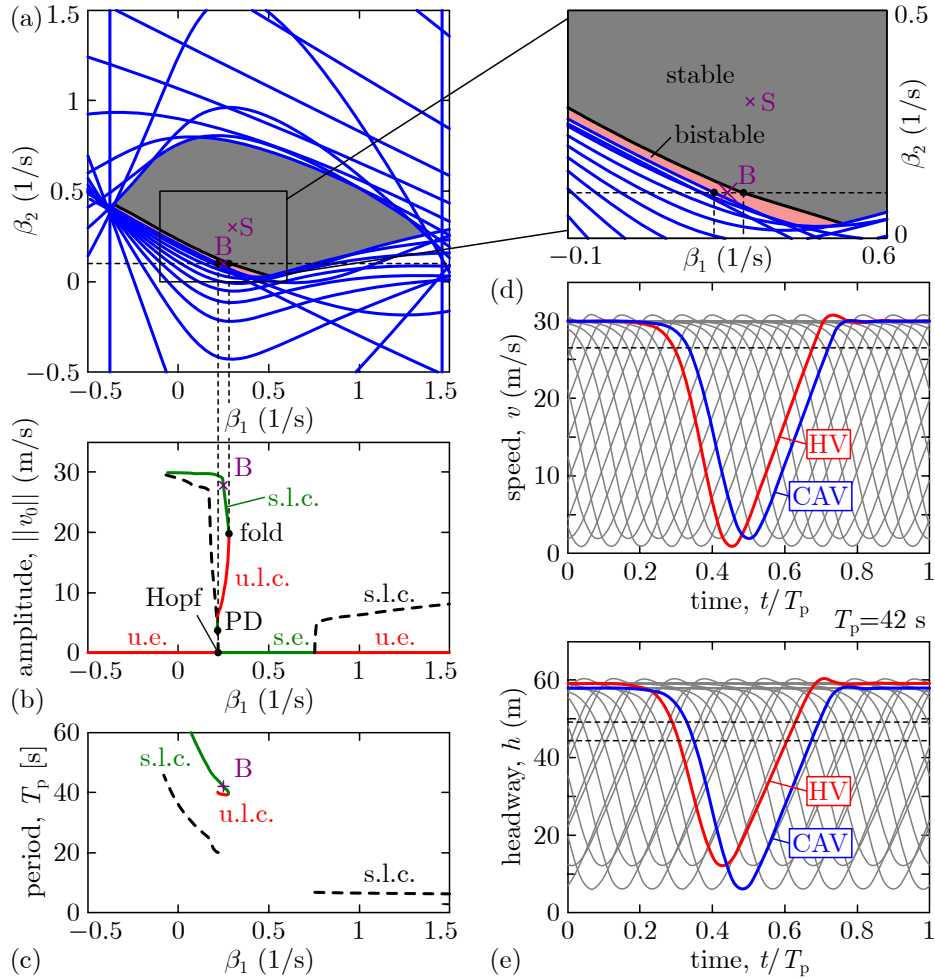
Figure 8 **Nonlinear dynamics of mixed traffic in ring configuration where every second vehicle is CAV (with** $m = 2$**). Compared to Figure 7, the higher penetration of connectivity and automation increases the size of the linearly stable region and decreases the relative size of the bistable region. This helps to eliminate traffic congestion phenomena and gives large freedom to select the controller parameters of CAVs. The rest of the parameters match those of Figure 4(c).**

The importance of connectivity is also highlighted by the stability charts presented above. Globally stable behavior is achievable only if the CAVs respond to the information from connectivity, that is, if $\beta_3 \neq 0$ in Figure 7 and $\beta_2 \neq 0$ in Figure 8. Note, however, that information from connectivity is available only if the CAVs travel in each other's communication range, which is a few hundred meters with current vehicle-to-vehicle connectivity technology. If the penetration of CAVs is very low and they are distributed sparsely in traffic, they may be too far from each other to communicate. As opposed, a higher penetration increases the chance of CAVs to communicate and helps eliminate instability or bistability phenomena.

The benefit of connectivity is further emphasized in Figure 10, where the scenario of Figure 9 is simulated without connectivity, considering non-connected automated vehicles (AVs) instead of CAVs. The AVs execute adaptive cruise control, obtained from the CCC strategy (9) with $\beta_j = 0$, $j > 1$, i.e., without
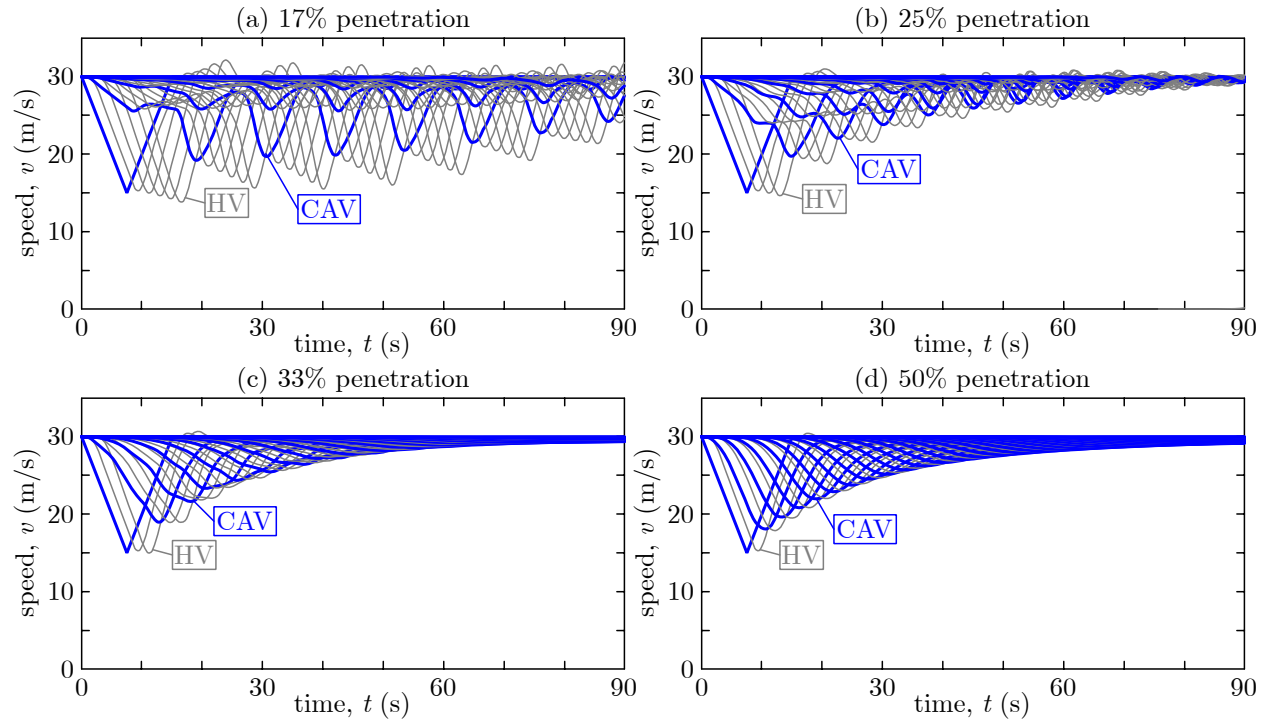
Figure 9 Simulation of mixed traffic where every mth vehicle is CAV (corresponding to $100/m$% penetration of connectivity and automation). Stable traffic flow is achieved despite the string unstable human driver behavior thanks to CAVs—even considering nonlinear dynamics. The parameters are **(a)** $m = 6$, **(b)** $m = 4$, **(c)** $m = 3$, **(d)** $m = 2$, and $\beta_1 = 0.3\,\text{s}^{-1}$, $\beta_m = 0.3\,\text{s}^{-1}$ **(related to point S in Figure 7(a) and Figure 8(a)). The rest of the parameters match those in Figure 7 and Figure 8.**

response to the vehicles farther ahead of the AVs. The remaining control gains α and β_1 are tuned to the best values found by the experiments in Beregi et al. (2023). According to Figure 10, AVs without connectivity fail to achieve stable mixed traffic unless the penetration of automation is very high (such as 50%). As opposed, moderate penetrations (such as 17%) of CAVs leveraging connectivity successfully smoothed out the traffic in Figure 9. These results show the promise of CAVs and the importance of connectivity to mitigate congestion in mixed traffic—ultimately leading to a more stable, smooth and safe future of mobility on highways.

5. Conclusions

In this paper, we analyzed the nonlinear dynamics of mixed traffic systems on highways, consisting of human-driven vehicles and connected automated vehicles (CAVs). We showed that homogeneous human-driven traffic is susceptible to phantom jams and bistability—an undesired phenomenon in which the same human drivers can both exhibit smooth driving behavior or cause a severe traffic congestion, depending on perturbations like an unexpected braking of an individual driver. To remedy this, we demonstrated that bistability and congestion can be mitigated by the positive impact of CAVs on mixed traffic, and we identified controller parameters for CAVs that are able to do so. Moreover, we highlighted that connectivity
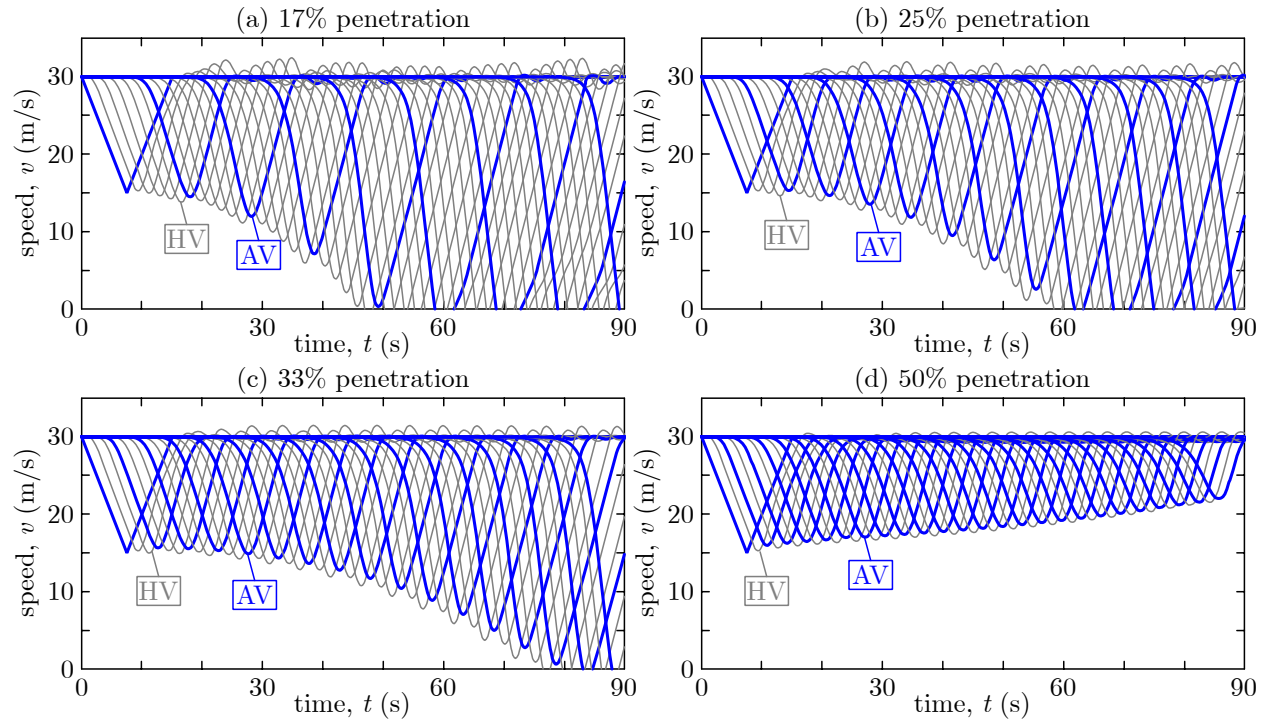
Figure 10   Simulation of mixed traffic where every mth vehicle is non-connected AV (corresponding to $100/m$% penetration of automation and no connectivity). Compared to Figure 9, much larger penetration of automation is required to achieve stable traffic flow, which highlights the importance of connectivity. The parameters are the same as in Figure 9, except $\beta_1 = 0.5\,\mathrm{s}^{-1}$ and $\beta_m = 0$.

between CAVs plays crucial role in mitigating the phantom jams caused by time delays and nonlinearities in the dynamics, while smooth mixed traffic is more challenging to achieve by automated vehicles without connectivity. Finally, we demonstrated that increasing the penetration of CAVs in mixed traffic further improves the nonlinear dynamic behavior and helps to avoid phantom jams caused by bistability.

Throughout this paper, we limited our discussion to a specific car-following model to describe human drivers and a specific connected cruise controller to regulate the motion of CAVs. We also restricted our numerical case studies to identical human drivers and identical CAVs, to reduce the number of underlying parameters. Nevertheless, our framework to explain congestion phenomena in mixed traffic—with the notions of bistabilty and phantom jams, and the tools of stability charts and bifurcation analysis—is applicable to other car-following models, other control strategies, and nonuniform driving behaviors too. The detailed analysis of these cases is left for future work. Future research directions also include analytical calculations to support the numerical analysis of bistability, and the extension of this work to multi-lane traffic scenarios and urban environments.
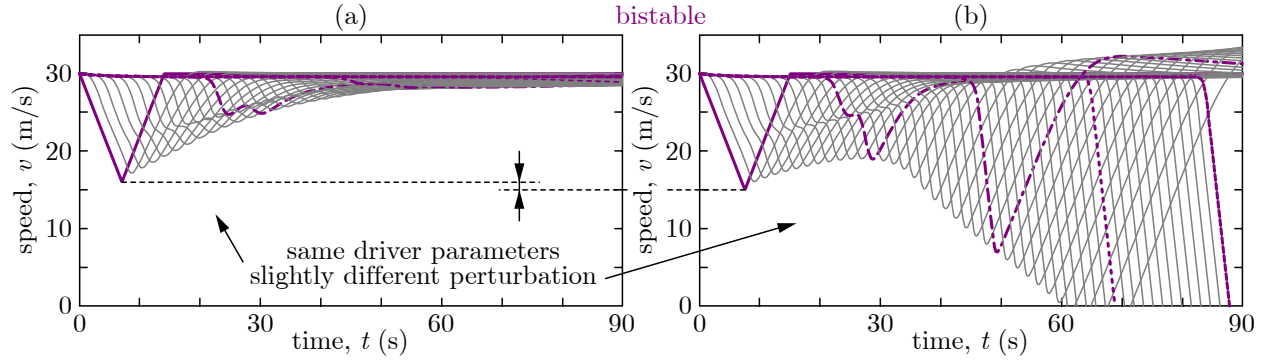
Acknowledgement

Figure 11 Simulation of human-driven traffic with the intelligent driver model. Similar to Figure 2(c,d), bistability is observed: smooth traffic and phantom jam are both possible for the same human drivers. The model (1), (5) and (19) was simulated with $a = 2\,\text{m/s}^2$, $b = 8\,\text{m/s}^2$, $v_{\max} = 36\,\text{m/s}$ and $T = 1.2\,\text{s}$, while setting the delay to $\tau_i = 0.9\,\text{s}$. The remaining parameters and the initial conditions are the same as in Figure 2(c,d).

Appendix A   Bistability with Various Human Driver Models

Figure 2(c,d) demonstrate bistable behavior and the occurrence of a phantom jam in human-driven traffic for a case where each HV is identical and described by the optimal velocity model (OVM). In this appendix, we highlight that bistability also occurs in case of other human driver models as well as in heterogeneous traffic where the HVs are nonidentical.

First, we demonstrate simulation results with the intelligent driver model (IDM) from Treiber et al. (2000):

$$f_i\left(h_i, v_i, \frac{\mathrm{d}h_i}{\mathrm{d}t}\right) = a\left(1 - \left(\frac{v_i}{v_{\max}}\right)^4 - \left(\frac{H\left(v_i, \frac{\mathrm{d}h_i}{\mathrm{d}t}\right)}{h_i}\right)^2\right),$$

$$H\left(v_i, \frac{\mathrm{d}h_i}{\mathrm{d}t}\right) = h_{\text{st}} + Tv_i - \frac{\mathrm{d}h_i}{\mathrm{d}t}\frac{v_i}{\sqrt{ab}},$$

(19)

where the parameters h_{st} and $v_{\max}$ have the same meaning as in the OVM, while a, b and T are additional driver parameters. Figure 11 shows the results of simulating the dynamics (1) and (5) of human-driven traffic with the IDM (19). Clearly, the same qualitative behavior is observed as in Figure 2(c,d): smooth traffic flow is recovered for a small speed perturbation, while a phantom jam occurs for a large one, indicating that the traffic system is bistable.

Next, we highlight that bistability and phantom jams occur for heterogeneous human-driven traffic. Figure 12 plots simulation results for the dynamics (1) and (5), considering nonidentical HVs described by the OVM (6) with driver parameters chosen randomly for each HV. The three rows of the figure showcase scenarios with three different sets of human driver parameters. Bistability arises in each case similar to Figure 2(c,d), and we observed this phenomenon consistently for several other random parameter sets too.
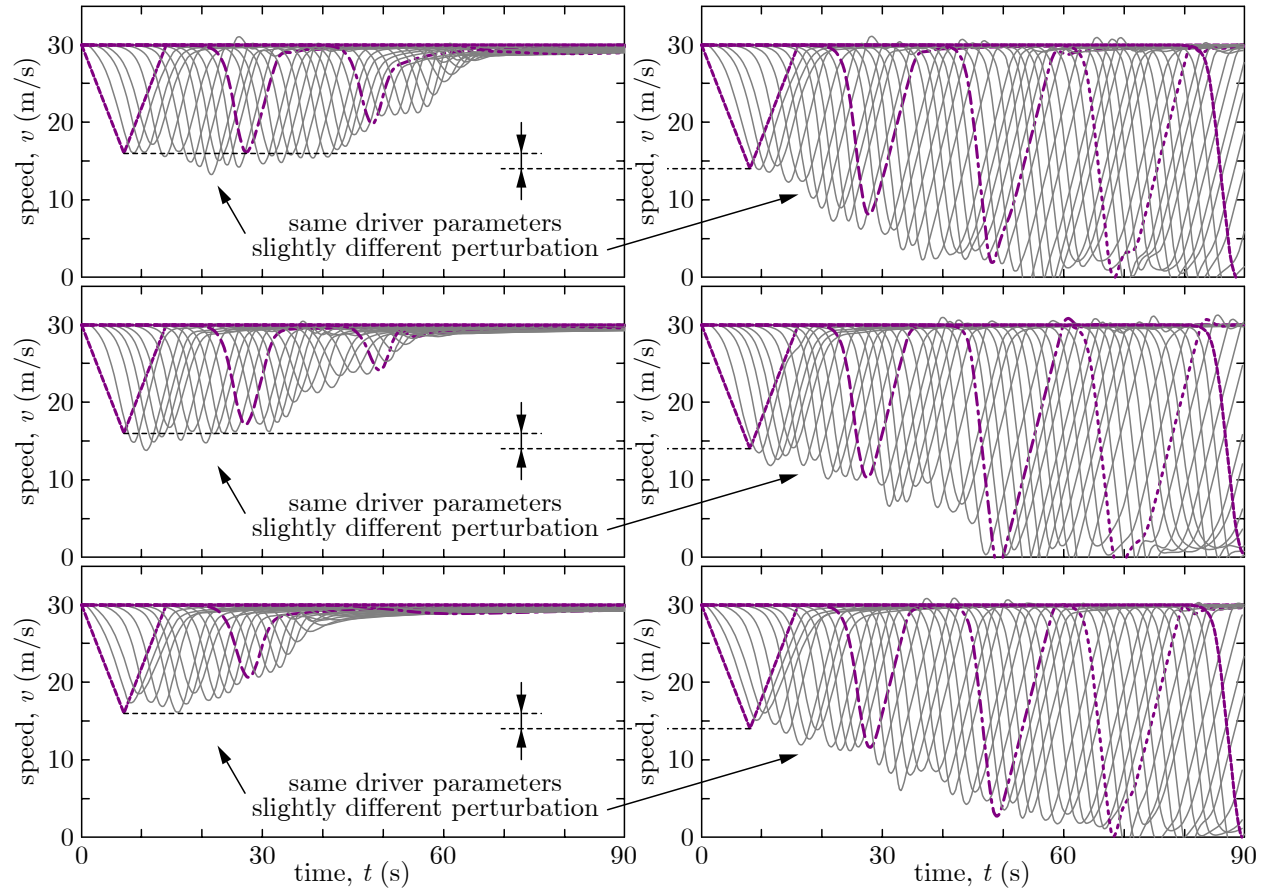
22

Molnar and Orosz: *Destroying Phantom Jams with Connectivity and Automation: Nonlinear Dynamics and Control of Mixed Traffic*
Article submitted to *Transportation Science*

Figure 12 **Simulation of heterogeneous human-driven traffic with three different sets of driver parameters.**
Bistability and phantom jams are observed in each case, similar to the homogeneous traffic with identical
HVs in Figure 2(c,d). The driver parameters are chosen for each HV randomly, from the intervals
$\alpha_{\mathrm{h}} \in [0.2, 0.6]\, 1/\mathrm{s}$**,** $\beta_{\mathrm{h}} \in [0.25, 0.75]\, 1/\mathrm{s}$ **and** $\tau_i \in [0.3, 0.9]\, \mathrm{s}$ **based on uniform distribution. The remaining parameters**
and the initial conditions are the same as in Figure 2(c,d).

These results highlight that, although the main body of the paper presents examples for identical human drivers described by the OVM, the phenomena of bistability and phantom jams are generic and occur for various human driver models and even for nonidentical HVs.

Molnar and Orosz: *Destroying Phantom Jams with Connectivity and Automation: Nonlinear Dynamics and Control of Mixed Traffic*
Article submitted to *Transportation Science*

23

Appendix B   Linear Stability Analysis

In this appendix, we discuss stability analysis for the linearized dynamics of mixed traffic, and we describe the analytical calculation of the linear stability charts in Figure 4.

B.1   Human-driven Traffic

First, we consider human-driven traffic on a ring, as illustrated by Figure 1(c). We consider N identical human drivers with delay $\tau_i = \tau$ for all $i \in I_{\mathrm{HV}}$ and with behavior governed by (1) and the OVM in (6). Within the saturation limits of sat and V_{h}, the corresponding linearized dynamics in (12) have the coefficients $A_{i,1} = \alpha_{\mathrm{h}} \kappa_{\mathrm{h}}$, $A_{i,2} = -\alpha_{\mathrm{h}}$ and $A_{i,3} = \beta_{\mathrm{h}}$, where $\kappa_{\mathrm{h}} = \frac{\mathrm{d}V_{\mathrm{h}}}{\mathrm{d}h}(h_{\mathrm{h}}^*)$. By the Laplace transformation of (12), we obtain the link transfer function in (14) in the form:

$$T_{i,i+1}(s) = \frac{A_{i,3}s + A_{i,1}}{s^2 \mathrm{e}^{s\tau} + (A_{i,3} - A_{i,2})s + A_{i,1}} = \frac{\beta_{\mathrm{h}}s + \alpha_{\mathrm{h}}\kappa_{\mathrm{h}}}{s^2 \mathrm{e}^{s\tau} + (\alpha_{\mathrm{h}} + \beta_{\mathrm{h}})s + \alpha_{\mathrm{h}}\kappa_{\mathrm{h}}}, \tag{20}$$

for all $i \in I_{\mathrm{HV}}$.

Since the ring consists of N identical HVs, the head-to-tail transfer function in (17) reads:

$$G_{0,N}(s) = \prod_{i \in I_{\mathrm{HV}}} T_{i,i+1}(s) = T_{i,i+1}(s)^N. \tag{21}$$

Therefore, the characteristic equation (18) of the ring becomes:

$$T_{i,i+1}(s) = \mathrm{e}^{-\mathrm{j}\frac{2k\pi}{N}}, \tag{22}$$

where $k \in \{0, 1, \ldots, N-1\}$ is called the wave number. After substituting (20), this leads to:

$$s^2 \mathrm{e}^{s\tau} + (\alpha_{\mathrm{h}} + \beta_{\mathrm{h}})s + \alpha_{\mathrm{h}}\kappa_{\mathrm{h}} - (\beta_{\mathrm{h}}s + \alpha_{\mathrm{h}}\kappa_{\mathrm{h}})\mathrm{e}^{\mathrm{j}\frac{2k\pi}{N}} = 0. \tag{23}$$

For each value of k, this equation can be solved for s and characteristic roots can be calculated, denoted by s_ℓ, $\ell \in \mathbb{Z}$. These roots must lie in the left half of the complex plane to achieve stability. Note that for $k = 0$ we have the root $s_0 = 0$, which represents the ring's translational symmetry. Hence we consider the remaining roots only and determine whether $\mathrm{Re}(s_\ell) < 0$ holds.

More precisely, we calculate the stability boundaries where $\mathrm{Re}(s_\ell) = 0$ holds for some $\ell \in \mathbb{Z} \backslash \{0\}$. These boundaries are formulated as curves in the space $(\beta_{\mathrm{h}}, \alpha_{\mathrm{h}})$ of parameters. To obtain these boundaries, we substitute $s = \mathrm{j}\omega$ into (23), where $\mathrm{j}^2 = -1$ and $\omega \geq 0$. For $\omega = 0$, we obtain $\alpha_{\mathrm{h}} = 0$ as stability boundary. For $\omega > 0$, we decompose (23) into real and imaginary parts, and solve the resulting two equations for β_{h} and α_{h}. For $k = 0$, this yields $\alpha_{\mathrm{h}} = (-1)^q \frac{(2q+1)\pi}{2\tau}$, $q \in \mathbb{Z}$. For $k > 0$, this leads to stability boundaries that are parameterized by $\omega > 0$:

$$\begin{aligned}
\alpha_{\mathrm{h}} &= \frac{\omega^2 \left(\cos(\omega\tau) - \cos\left(\omega\tau - \frac{2k\pi}{N}\right)\right)}{-\omega \sin\frac{2k\pi}{N} + 2\kappa_{\mathrm{h}}\left(1 - \cos\frac{2k\pi}{N}\right)}, \\
\beta_{\mathrm{h}} &= \frac{-\omega^2 \cos(\omega\tau) + \kappa_{\mathrm{h}}\omega\left(\sin(\omega\tau) - \sin\left(\omega\tau - \frac{2k\pi}{N}\right)\right)}{-\omega \sin\frac{2k\pi}{N} + 2\kappa_{\mathrm{h}}\left(1 - \cos\frac{2k\pi}{N}\right)}.
\end{aligned} \tag{24}$$

The stability boundaries are plotted in Figure 4(a) for each value of k, resulting in the blue curves bounding the linearly stable parameter region.

24

Molnar and Orosz: *Destroying Phantom Jams with Connectivity and Automation: Nonlinear Dynamics and Control of Mixed Traffic*
Article submitted to *Transportation Science*

B.2 Mixed Traffic

Next, we consider mixed traffic on a ring with N vehicles where every mth vehicle is CAV while the others are HVs; see Figure 1(d). That is, a group of m vehicles (one CAV and $m-1$ HVs) is repeated N/m times along the ring, where N/m is considered to be an integer. Each HV is assumed to be identical, as described above. Furthermore, the CAVs are also identical, executing the CCC (9) with delay $\tau_i = \sigma$ for all $i \in I_{\mathrm{CAV}}$. Within the saturation limits of sat, V and W, the linearized dynamics (13) have the coefficients $A_{i,1} = \alpha\kappa$, $A_{i,2} = -\alpha - \sum_{j=1}^{m} \beta_j$ and $A_{i,j+2} = \beta_j$, where $\kappa = \frac{\mathrm{d}V}{\mathrm{d}h}(h^*)$. The link transfer functions describing the CAVs in (15) read:

$$
\begin{aligned}
T_{i,i+1}(s) &= \frac{A_{i,3}s + A_{i,1}}{s^2\mathrm{e}^{s\sigma} - A_{i,2}s + A_{i,1}} = \frac{\beta_1 s + \alpha\kappa}{s^2\mathrm{e}^{s\sigma} + \left(\alpha + \sum_{j=1}^{m}\beta_j\right)s + \alpha\kappa}, \\
T_{i,i+j}(s) &= \frac{A_{i,j+2}s}{s^2\mathrm{e}^{s\sigma} - A_{i,2}s + A_{i,1}} = \frac{\beta_j s}{s^2\mathrm{e}^{s\sigma} + \left(\alpha + \sum_{j=1}^{m}\beta_j\right)s + \alpha\kappa}, \quad j \in \{2,\dots,m\},
\end{aligned}
\tag{25}
$$

for all $i \in I_{\mathrm{CAV}}$. The link transfer functions describing HVs are still given by (20) for all $i \in I_{\mathrm{HV}}$.

We assume that each CAV responds to the vehicle immediately ahead of them and to the preceding CAV m vehicles ahead, that is, β_1 and β_m are nonzero while $\beta_j = 0$ for $j \in \{2,\dots,m-1\}$. Then, the response of the m-vehicle group, that comprises the CAV and the $m-1$ preceding HVs, is described by the head-to-tail transfer function:

$$
G_{i,i+m}(s) = T_{i,i+1}(s) \prod_{j=1}^{m-1} T_{i+j,i+j+1}(s) + T_{i,i+m}(s),
\tag{26}
$$

for all $i \in I_{\mathrm{CAV}}$.

Since the group of m vehicles is repeated N/m times along the ring, the head-to-tail transfer function of the overall ring configuration in (17) becomes:

$$
G_{0,N}(s) = \prod_{i \in I_{\mathrm{CAV}}} G_{i,i+m}(s) = G_{i,i+m}(s)^{N/m}.
\tag{27}
$$

Therefore, the characteristic equation (18) takes the form:

$$
G_{i,i+m}(s) = \mathrm{e}^{-\mathrm{j}\frac{2k\pi m}{N}},
\tag{28}
$$

with $k \in \{0,1,\dots,N/m-1\}$. After substituting (25), this leads to:

$$
s^2\mathrm{e}^{s\sigma} + (\alpha + \beta_1 + \beta_m)s + \alpha\kappa - \left((\beta_1 s + \alpha\kappa)G_{i+1,i+m}(s) + \beta_m s\right)\mathrm{e}^{\mathrm{j}\frac{2k\pi m}{N}} = 0,
\tag{29}
$$

where $G_{i+1,i+m}(s) = \prod_{j=1}^{m-1} T_{i+j,i+j+1}(s)$ denotes the overall response of the $m-1$ HVs. The stability of the ring configuration can be analyzed by investigating the roots of the characteristic equation (29). Again, notice that for $k=0$ we have the root $s_0 = 0$ (since $G_{i+1,i+m}(0) = 1$ holds), which represents the ring's translational symmetry and is disregarded for the subsequent analysis.

We calculate the stability boundaries as curves in the space (β_1, β_m) of control gains. To this end, we substitute $s = j\omega$ into (29). For $\omega = 0$, we obtain $\alpha = 0$ as stability boundary which does not show up as a curve in the (β_1, β_m) space. For $\omega > 0$, we decompose (29) into real and imaginary parts, and solve it for β_1 and β_m. For $k = 0$, we get:

$$\beta_1 = \frac{\omega^2 \cos(\omega\sigma) - \alpha\kappa(1 - \Gamma_{\mathrm{R}})}{\omega\Gamma_{\mathrm{I}}}, \tag{30}$$

where $\Gamma_{\mathrm{R}} = \mathrm{Re}(G_{i+1,i+m}(j\omega))$, $\Gamma_{\mathrm{I}} = \mathrm{Im}(G_{i+1,i+m}(j\omega))$ and ω is the solution of:

$$-\omega^2\left((1 - \Gamma_{\mathrm{R}})\cos(\omega\sigma) - \Gamma_{\mathrm{I}}\sin(\omega\sigma)\right) + \alpha\kappa\left((1 - \Gamma_{\mathrm{R}})^2 + \Gamma_{\mathrm{I}}^2\right) - \alpha\omega\Gamma_{\mathrm{I}} = 0. \tag{31}$$

For $k > 0$, we obtain the following stability boundaries parameterized by $\omega > 0$:

$$\beta_1 = \frac{\omega^2\left(\cos(\omega\sigma) - \cos\left(\omega\sigma - \frac{2k\pi m}{N}\right)\right) + \alpha\omega S - \alpha\kappa\left((\Gamma_{\mathrm{R}} + 1)(1 - C) + \Gamma_{\mathrm{I}}S\right)}{\omega\left((\Gamma_{\mathrm{R}} - 1)S - \Gamma_{\mathrm{I}}(1 - C)\right)},$$

$$\beta_m = \frac{-\omega^2\left(\cos(\omega\sigma) - \Gamma_{\mathrm{R}}\cos\left(\omega\sigma - \frac{2k\pi m}{N}\right) - \Gamma_{\mathrm{I}}\sin\left(\omega\sigma - \frac{2k\pi m}{N}\right)\right)}{\omega\left((\Gamma_{\mathrm{R}} - 1)S - \Gamma_{\mathrm{I}}(1 - C)\right)} \tag{32}$$

$$+ \frac{-\alpha\omega\left(\Gamma_{\mathrm{R}}S + \Gamma_{\mathrm{I}}C\right) + \alpha\kappa\left(1 - 2\Gamma_{\mathrm{R}}C + 2\Gamma_{\mathrm{I}}S + \Gamma_{\mathrm{R}}^2 + \Gamma_{\mathrm{I}}^2\right)}{\omega\left((\Gamma_{\mathrm{R}} - 1)S - \Gamma_{\mathrm{I}}(1 - C)\right)},$$

where $S = \sin\frac{2k\pi m}{N}$ and $C = \cos\frac{2k\pi m}{N}$. The stability boundaries are plotted as the blue curves in Figure 4(b,c) for each value of k, considering $m = 3$ and $m = 2$.

References

Alan A, He CR, Molnar TG, Mathew JC, Bell AH, Orosz G (2024) Integrating safety with performance in connected automated truck control: Experimental validation. *IEEE Transactions on Intelligent Vehicles* 9(1):3075–3088, URL http://dx.doi.org/10.1109/TIV.2023.3305204.

Ames AD, Xu X, Grizzle JW, Tabuada P (2017) Control barrier function based quadratic programs for safety critical systems. *IEEE Transactions on Automatic Control* 62(8):3861–3876, URL http://dx.doi.org/10.1109/TAC.2016.2638961.

Avedisov SS, Bansal G, Orosz G (2022) Impacts of connected automated vehicles on freeway traffic patterns at different penetration levels. *IEEE Transactions on Intelligent Transportation Systems* 5(23):4305–4318, URL http://dx.doi.org/10.1109/TITS.2020.3043323.

Bando M, Hasebe K, Nakanishi K, Nakayama A (1998) Analysis of optimal velocity model with explicit delay. *Physical Review E* 58(5):5429–5435, URL http://dx.doi.org/10.1103/PhysRevE.58.5429.

Bekiaris-Liberis N, Roncoli C, Papageorgiou M (2018) Predictor-based adaptive cruise control design. *IEEE Transactions on Intelligent Transportation Systems* 19(10):3181–3195, URL http://dx.doi.org/10.1109/TITS.2017.2771501.

Beregi S, Avedisov SS, He CR, Takács D, Orosz G (2023) Connectivity-based delay-tolerant control of automated vehicles: Theory and experiments. *IEEE Transactions on Intelligent Vehicles* 8(1):275–289, URL http://dx.doi.org/10.1109/TIV.2021.3131957.

Beregi S, Takacs D, Stepan G (2019) Bifurcation analysis of wheel shimmy with non-smooth effects and time delay in the tyre–ground contact. *Nonlinear Dynamics* 98(1):841–858, URL http://dx.doi.org/10.1007/s11071-019-05123-1.

Bertoni L, Guanetti J, Basso M, Masoero M, Cetinkunt S, Borrelli F (2017) An adaptive cruise control for connected energy-saving electric vehicles. *IFAC-PapersOnLine* 50(1):2359–2364, URL http://dx.doi.org/10.1016/j.ifacol.2017.08.425.

Čičić M, Johansson KH (2018) Traffic regulation via individually controlled automated vehicles: a cell transmission model approach. *21st IEEE International Conference on Intelligent Transportation Systems*, 766–771, URL http://dx.doi.org/10.1109/ITSC.2018.8569960.

Cui S, Seibold B, Stern R, Work DB (2017) Stabilizing traffic flow via a single autonomous vehicle: Possibilities and limitations. *IEEE Intelligent Vehicles Symposium*, 1336–1341, URL http://dx.doi.org/10.1109/IVS.2017.7995897.

Dombovari Z, Wilson RE, Stepan G (2008) Estimates of the bistable region in metal cutting. *Proceedings of the Royal Society A* 464:3255–3271, URL http://dx.doi.org/10.1098/rspa.2008.0156.

Engelborghs K, Luzyanina T, Roose D (2002) Numerical bifurcation analysis of delay differential equations using DDE-BIFTOOL. *ACM Transactions on Mathematical Software* 28(1):1–21, URL http://dx.doi.org/10.1145/513001.513002.

Molnar and Orosz: *Destroying Phantom Jams with Connectivity and Automation: Nonlinear Dynamics and Control of Mixed Traffic*
Article submitted to *Transportation Science*

27

Ge JI, Avedisov SS, He CR, Qin WB, Sadeghpour M, Orosz G (2018) Experimental validation of connected automated vehicle design among human-driven vehicles. *Transportation Research Part C* 91:335–352, URL `http://dx.doi.org/10.1016/j.trc.2018.04.005`.

Ge JI, Orosz G (2014) Dynamics of connected vehicle systems with delayed acceleration feedback. *Transportation Research Part C* 46:46–64, URL `http://dx.doi.org/10.1016/j.trc.2014.04.014`.

Giammarino V, Baldi S, Frasca P, Monache MLD (2021) Traffic flow on a ring with a single autonomous vehicle: An interconnected stability perspective. *IEEE Transactions on Intelligent Transportation Systems* 22(8):4998–5008, URL `http://dx.doi.org/10.1109/TITS.2020.2985680`.

Giammarino V, Lv M, Baldi S, Frasca P, Delle Monache ML (2019) On a weaker notion of ring stability for mixed traffic with human-driven and autonomous vehicles. *58th IEEE Conference on Decision and Control*, 335–340, URL `http://dx.doi.org/10.1109/CDC40024.2019.9029529`.

Guckenheimer J, Holmes P (1983) *Nonlinear Oscillations, Dynamical Systems, and Bifurcations of Vector Fields*, volume 42 of *Applied Mathematical Sciences* (Springer), URL `http://dx.doi.org/10.1007/978-1-4612-1140-2`.

Gunter G, Gloudemans D, Stern RE, McQuade S, Bhadani R, Bunting M, Delle Monache ML, Lysecky R, Seibold B, Sprinkle J, Piccoli B, Work DB (2021) Are commercially implemented adaptive cruise control systems string stable? *IEEE Transactions on Intelligent Transportation Systems* 22(11):6992–7003, URL `http://dx.doi.org/10.1109/TITS.2020.3000682`.

Hayat A, Gong X, Lee J, Truong S, McQuade S, Kardous N, Keimer A, You Y, Albeaik S, Vinistky E, Arnold P, Delle Monache ML, Bayen A, Seibold B, Sprinkle J, Work D, Piccoli B (2022) A holistic approach to the energy-efficient smoothing of traffic via autonomous vehicles. Blondin MJ, Fernandes Trovão JP, Chaoui H, Pardalos PM, eds., *Intelligent Control and Smart Energy Management: Renewable Resources and Transportation*, 285–316 (Springer), URL `http://dx.doi.org/10.1007/978-3-030-84474-5_10`.

Kiss AK, Avedisov SS, Bachrathy D, Orosz G (2019) On the global dynamics of connected vehicle systems. *Nonlinear Dynamics* 96(3):1865–1877, URL `http://dx.doi.org/10.1007/s11071-019-04889-8`.

Lichtlé N, Vinitsky E, Nice M, Seibold B, Work D, Bayen AM (2022) Deploying traffic smoothing cruise controllers learned from trajectory data. *International Conference on Robotics and Automation*, 2884–2890, URL `http://dx.doi.org/10.1109/ICRA46639.2022.9811912`.

McAuliffe B, Lammert M, Lu XY, Shladover S, Surcel MD, Kailas A (2018) Influences on energy savings of heavy trucks using cooperative adaptive cruise control. *WCX World Congress Experience* (SAE International), URL `http://dx.doi.org/10.4271/2018-01-1181`.

Molnár TG, Hopka M, Upadhyay D, Van Nieuwstadt M, Orosz G (2023) Virtual rings on highways: Traffic control by connected automated vehicles. Murphey YL, Kolmanovsky I, Watta P, eds., *AI-enabled Technologies for Autonomous and Connected Vehicles*, 441–479 (Springer), URL `http://dx.doi.org/10.1007/978-3-031-06780-8_16`.

Molnár TG, Insperger T, John Hogan S, Stépán G (2016) Estimation of the bistable zone for machining operations for the case of a distributed cutting-force model. *Journal of Computational and Nonlinear Dynamics* 11(5):051008, URL http://dx.doi.org/10.1115/1.4032443.

Nilsson P, Hussien O, Balkan A, Chen Y, Ames AD, Grizzle JW, Ozay N, Peng H, Tabuada P (2016) Correct-by-construction adaptive cruise control: Two approaches. *IEEE Transactions on Control Systems Technology* 24(4):1294–1307, URL http://dx.doi.org/10.1109/TCST.2015.2501351.

Orosz G (2016) Connected cruise control: modeling, delay effects, and nonlinear behavior. *Vehicle System Dynamics* 54(8):1147–1176, URL http://dx.doi.org/10.1080/00423114.2016.1193209.

Orosz G, Stépán G (2006) Subcritical Hopf bifurcations in a car-following model with reaction-time delay. *Proceedings of the Royal Society A* 2073(462):2643–2670, URL http://dx.doi.org/10.1098/rspa.2006.1660.

Orosz G, Wilson RE, Stépán G (2010) Traffic jams: dynamics and control. *Philosophical Transactions of the Royal Society A* 368(1928):4455–4479, URL http://dx.doi.org/10.1098/rsta.2010.0205.

Orosz G, Wilson RE, Szalai R, Stépán G (2009) Exciting traffic jams: Nonlinear phenomena behind traffic jam formation on highways. *Physical Review E* 80(4):046205, URL http://dx.doi.org/10.1103/PhysRevE.80.046205.

Qin W (2022) A nonlinear car-following controller design inspired by human-driving behaviors to increase comfort and enhance safety. *IEEE Transactions on Vehicular Technology* 8(71):8212–8224, URL http://dx.doi.org/10.1109/TVT.2022.3175746.

Saha A, Wahi P (2011) Delayed feedback for controlling the nature of bifurcations in friction-induced vibrations. *Journal of Sound and Vibration* 330(25):6070–6087, URL http://dx.doi.org/10.1016/j.jsv.2011.07.032.

Sieber J, Engelborghs K, Luzyanina T, Samaey G, Roose D (2014) DDE-Biftool Manual - Bifurcation analysis of delay differential equations. *arXiv preprint, arXiv:1406.7144* URL http://dx.doi.org/10.48550/arXiv.1406.7144.

Stern RE, Cui S, Delle Monache ML, Bhadani R, Bunting M, Churchill M, Hamilton N, Haulcy R, Pohlmann H, Wu F, Piccoli B, Seibold B, Sprinkle J, Work DB (2018) Dissipation of stop-and-go waves via control of autonomous vehicles: Field experiments. *Transportation Research Part C* 89:205–221, URL http://dx.doi.org/10.1016/j.trc.2018.02.005.

Treiber M, Hennecke A, Helbing D (2000) Congested traffic states in empirical observations and microscopic simulations. *Physical Review E* 62:1805–1824, URL http://dx.doi.org/10.1103/PhysRevE.62.1805.

Turri V, Besselink B, Johansson KH (2017) Cooperative look-ahead control for fuel-efficient and safe heavy-duty vehicle platooning. *IEEE Transactions on Control Systems Technology* 25(1):12–28, URL http://dx.doi.org/10.1109/TCST.2016.2542044.

Molnar and Orosz: *Destroying Phantom Jams with Connectivity and Automation: Nonlinear Dynamics and Control of Mixed Traffic*
Article submitted to *Transportation Science*

29

van Nunen E, Reinders J, Semsar-Kazerooni E, van de Wouw N (2019) String stable model predictive cooperative adaptive cruise control for heterogeneous platoons. *IEEE Transactions on Intelligent Vehicles* 4(2):186–196, URL http://dx.doi.org/10.1109/TIV.2019.2904418.

Veraszto Z, Stepan G (2017) Nonlinear dynamics of hardware-in-the-loop experiments on stick–slip phenomena. *International Journal of Non-Linear Mechanics* 94:380–391, URL http://dx.doi.org/10.1016/j.ijnonlinmec.2017.01.006.

von Allwörden H, Gasser I (2021) On a general class of solutions for an optimal velocity model on an infinite lane. *Transportmetrica A: Transport Science* 17(3):258–277, URL http://dx.doi.org/10.1080/23249935.2020.1778813.

Vörös I, Orosz G, Takács D (2023) On the global dynamics of path-following control of automated passenger vehicles. *Nonlinear Dynamics* 111(9):8235–8252, URL http://dx.doi.org/10.1007/s11071-023-08284-2.

Wang S, Stern R, Levin MW (2022) Optimal control of autonomous vehicles for traffic smoothing. *IEEE Transactions on Intelligent Transportation Systems* 23(4):3842–3852, URL http://dx.doi.org/10.1109/TITS.2021.3094552.

Wang Y, Wang Z, Han K, Tiwari P, Work DB (2021) Personalized adaptive cruise control via Gaussian process regression. *24th IEEE International Conference on Intelligent Transportation Systems*, 1496–1502, URL http://dx.doi.org/10.1109/ITSC48978.2021.9564498.

Wang Z, Wu G, Barth MJ (2018) A review on cooperative adaptive cruise control (CACC) systems: Architectures, controls, and applications. *21st IEEE International Conference on Intelligent Transportation Systems*, 2884–2891, URL http://dx.doi.org/10.1109/ITSC.2018.8569947.

Yu H, Krstic M (2022) *Traffic Congestion Control by PDE Backstepping* (Birkhäuser), URL http://dx.doi.org/10.1007/978-3-031-19346-0.

Zhang L, Orosz G (2016) Motif-based design for connected vehicle systems in presence of heterogeneous connectivity structures and time delays. *IEEE Transactions on Intelligent Transportation Systems* 17(6):1638–1651, URL http://dx.doi.org/10.1109/TITS.2015.2509782.

Zheng Y, Wang J, Li K (2020) Smoothing traffic flow via control of autonomous vehicles. *IEEE Internet of Things Journal* 7(5):3882–3896, URL http://dx.doi.org/10.1109/JIOT.2020.2966506.